



The impacts of multi-physics parameterization on forecasting heavy rainfall induced by weak landfalling Typhoon Rumbia (2018)

Yiting Zhu^{a,c,d}, Fengxue Qiao^{a,b,c,d,*}, Yujia Liu^{a,b}, Xin-Zhong Liang^e, Qiyang Liu^{a,c,d}, Rui Wang^f, Han Zhang^g

^a Key Laboratory of Geographic Information Science, Ministry of Education, East China Normal University, Shanghai 200241, China

^b State Key Laboratory of Numerical Modeling for Atmospheric Sciences and Geophysical Fluid Dynamics, Institute of Atmospheric Physics, Chinese Academy of Sciences, Beijing, China

^c Institute of Eco-Chongming (IEC), Shanghai 200062, China

^d Joint Laboratory for Environmental Remote Sensing and Data Assimilation, ECNU & CEODE, Shanghai 200241, China

^e Earth System Science Interdisciplinary Center, University of Maryland, MD, USA

^f Shanghai Central Meteorological Observatory, Shanghai 200030, China

^g College of Atmospheric Science, Nanjing University of Information Science and Technology, Nanjing, China



ARTICLE INFO

Keywords:

Heavy rainfall distribution

Microphysics parameterizations

Planetary boundary layer schemes

ABSTRACT

The weak and sustained tropical cyclone (TC) Rumbia (2018) and its associated heavy precipitation after landfall are simulated by the Weather Research and Forecasting model using three microphysics parameterizations (MP) and two planetary boundary layer (PBL) schemes. Key factors regulating the heavy rainfall distribution of landed TC at three stages (landfall, inland slow-moving and recurring stage) and their sensitivities to multi-physics parameterizations are examined. Results show that heavy rainfall distribution is largely regulated by the intensity of TC itself at landfall, but more affected by environmental factors at the two inland stages, including the environmental vertical wind shear, the associated upper-level wind divergence and low-level moisture convergence. Different MP and PBL schemes mainly affect the simulation of TC thermodynamic structure and key environmental factors, leading to their different forecast skills at three stages. Specifically, the Yonsei University (YSU) PBL scheme systematically outperforms the Mellor-Yamada-Nakanishi-Niino (MYNN) scheme in simulating stronger TC and heavy rainfall intensity. With the advantageous YSU PBL scheme, the Ferrier MP scheme only shows a slight advantage in simulating the intensity of TC and heavy rainfall at landfall. However, the WRF single-moment 6-class (WSM6) and Thompson scheme produce more graupel or snow, and better simulate the key environmental factors, showing their respective advantages in simulating the heavy rainfall structure and location at the two inland stages. This implies that the use of nonlocal YSU PBL scheme and the MP schemes with sophisticated ice processes shows superiority in simulating the postlandfall heavy rainfall induced by weak TCs.

1. Introduction

Strong tropical cyclones (TCs) usually cause heavy rainfall and bring great losses near the coastal regions during landfall, but some weak landfalling TCs and their remnants can also bring extensive and widespread heavy rainfall after moving farther inland, resulting in unexpected devastating damages (Chen and Ding, 1979; Jones et al., 2003; Meng and Wang, 2016a, 2016b). For instance, the most notable disaster of 1975 ("75.8") TC flooding in Henan was caused by the remnant of landfalling TC Nina (1975). It made its landfall as a weakened tropical storm in southeast China but brought heavy rainfall and flash flooding as

it moved farther inland, leading to the collapse of reservoirs and deadly disasters (Chen and Ding, 1979). Typhoon Rumbia (2018), which was just a tropical storm at landfall in Shanghai, China, on 17 August, persisted for about 4 days inland and caused record-breaking extreme rainfall along its way inland across the East and Central China. Thus, the study of heavy rainfall associated with weak TCs after its landfall is worthy of attention, which is particularly crucial for disaster prevention and risk mitigations.

However, it has been always a great challenge to accurately predict the rainfall distribution induced by landfalling TCs. Difficulties mainly arise from the inadequate understanding of TC precipitation

* Corresponding author at: School of Geographic Sciences, East China Normal University, 500 Dongchuan Road, Shanghai 200241, China.

E-mail address: fxqiao@geo.ecnu.edu.cn (F. Qiao).

mechanisms and the improper model physics representations. Most studies have shown that the rainfall associated with landfalling TCs is controlled by complex multi-scale interactions, and exhibits highly asymmetric distribution with variable small-scale features (Colle, 2003; May et al., 2008; Meng and Wang, 2016a, 2016b). Various factors and physical mechanisms have been proposed to explain the landfalling TC rainfall asymmetries, including the TC intensity (Feng and Shu, 2018), surface friction-induced boundary layer convergence and TC motion (Li et al., 2015; Xu et al., 2014; Yu et al., 2015), environmental vertical wind shear (VWS; Feng and Shu, 2018), interaction of the TC circulation with westerly baroclinic systems or monsoon flows (Meng and Wang, 2016b), the Mesoscale Convective Systems (MCSs) embedded in the TC circulation (Cecil, 2007), and local small-scale topographic effects (Yu et al., 2010; Yu et al., 2017). Their specific roles and relative importance have not yet been fully understood for heavy rainfall induced by landfalling TCs.

Recently, more attention has been paid to the impact of TC intensity and environmental VWS. The rainfall asymmetry was found to increase with the environmental VWS strength but decrease with the TC intensity (Chen et al., 2006; Cecil, 2007). Specifically, the TC intensity affects more the rainfall distribution within the TC core region, while the environmental VWS primarily affects the outer rainbands which might have larger rain rates than the inner core for TCs moving inland (Chen et al., 2006; Hence and Houze, 2012; Yu et al., 2010). However, there is no clear relationship between heavy rainfall distribution and storm intensity for landfalling TCs (Lonfat et al., 2004; Yu et al., 2015; Yu et al., 2017), and most studies identified the downshear or downshear-left rainfall maxima to the environmental VWS for landfalling TCs over the South and East China (Feng and Shu, 2018; Gao et al., 2009; Wang and Holland, 1996; Yu et al., 2015; Yu et al., 2010). Then continuous efforts have been put on the impact of environment system and its interaction with TC circulations. For instance, the western North Pacific Subtropical High (WNPSH) mainly inhibits the convection of TC in the VWS upshear side through the intrusion of dry air (Feng and Shu, 2018; Shu et al., 2014); The strength of midlatitude systems affects the TC rainfall location (Atallah et al., 2007), increases the baroclinic instability and TC convection, which facilitate the rainfall enhancement and the maintenance of TC circulation inland (Komaromi and Doyle, 2018). Some studies also suggested that the interaction of the TC circulation with the intraseasonal oscillations induced monsoonal surges and the embedded MCSs greatly contributes to the post-landfall rainfall enhancement (Chen et al., 2010; Ge et al., 2010; Ling et al., 2016; Meng and Wang, 2016a; Wu et al., 2011).

Particularly for weak TCs at landfall, Feng and Shu (2018) suggested that the asymmetric distribution of heavy rainfall is affected more by the environmental factors than the storm intensity. They showed that such heavy rainfalls at landfall are accompanied by strong and tilted updrafts in TC vertical circulation, which are caused by strong environmental VWS and upper-level divergence under effective coupling of ambient synoptic systems. However, the heavy rainfall distribution and its favourable synoptic patterns can vary with landing stages. Therefore, we examine this typical case of Rumbia (2018) to better understand the specific environmental conditions for heavy rainfall associated with weak and sustained TCs at landfall and post-landfall stages.

Previous studies have examined the sensitivity of TC intensity and associated rainfall simulations to different physical processes, including cloud microphysics parameterization (MP; e.g., Fovell and Su, 2007; Sun et al., 2015; Tao et al., 2011) and planetary boundary layer (PBL; e.g., Wang, 2013; Kepert, 2012; Nolan et al., 2009a, 2009b) schemes. Although some pointed out that complex interaction of model physics plays an important role in TC intensity or precipitation forecast (Davis and Bosart, 2002; Li and Pu, 2008; McFarquhar et al., 2006; Nasrollahi et al., 2012; Fovell et al., 2016), no configuration was always significantly better, and it is still unclear about the physical processes through which these different model physics affect the heavy rainfall induced by weak long-lasting TCs after landfall.

Specifically, the MP schemes describe the conversion among different cloud hydrometeors associated with diabatic heating and cooling, while this process plays an important role on the TC structure and intensity (Chen et al., 2018). Observational studies showed that cloud hydrometeors and dominated precipitating processes differ in the inner and outer TC rainbands (Wu et al., 2018), and different MP schemes may be required in forecasting these convective rainbands because varied raindrop size distributions were observed in Typhoon Fitow (Bao et al., 2019). Numerical studies showed that the warm-rain-only MP scheme has stronger condensational heating and produces an earlier and more rapid TC intensification rate than the mixed-phase schemes (Willoughby et al., 1984; Lord and Lord, 1988; Wang, 2002; Tao et al., 2011). However, in the mixed-phase schemes, the evaporative and melting cooling of the raindrops and snow/graupeal mainly controls the TC outer rainbands and downdrafts, which adversely affects the TC intensity (Bender, 1997; Wang, 2002; Zhu and Zhang, 2006). For instance, Sun et al. (2015) found that the evaporative (melting) process of hydrometeors in the TC downdrafts may weaken the intensity of WNPSH nearby and thus the TC activities. Among various MP schemes in the WRF model, the Ferrier (NOAA, 2010) and Thompson (Thompson et al., 2008) scheme showed specific advantages in predicting the track and intensity of landed TCs over different regions, such as the former in the Bay of Bengal (Raju et al., 2011) and the South China Sea (Chen et al., 2015), and the latter in the Atlantic oceans (Jin et al., 2014). While in the series of WSM schemes, the WSM6 scheme most realistically reproduced the melting process of snow and graupel in TC Mujigae (2015) shown by Pang et al. (2019). Therefore, we focus on Ferrier, Thompson and WSM6 schemes with different ice processes to examine the mixed-phased MP impacts.

Numerous studies have suggested that TC intensity, structure or rainfall are sensitive to PBL parameterizations (Braun and Tao, 2000; Dong et al., 2019; Li and Pu, 2008; Liu et al., 2017; Smith and Thomsen, 2010; Wang, 2013; Kepert, 2012; Nolan et al., 2009a, 2009b; Zhang et al., 2015; Zhang and Rogers, 2019), but controversies still existed. For instance, the first-order nonlocal scheme of Yonsei University (YSU, Hong et al., 2006) showed superiority in predicting the intensity, track and rainfall for Typhoon Muifa (2011) over the Medium-Range Forecast (MRF) scheme in the study of Wang (2013), while the higher-order local Mellor-Yamada-Janic (MYJ, Janjić, 1994) scheme outperformed the YSU scheme in simulating the rapid intensification process of Hurricane Katrina (2005) before its landfall (Liu et al., 2017). However, Dong et al. (2019) showed that YSU outperformed the higher-order local Mellor-Yamada-Nakanishi-Niino (MYNN) Level 2.5 (Mellor and Yamada, 1982; Nakanishi and Niino, 2006, 2009) and the MYJ scheme in predicting the rainfall after landfall of Typhoon Fitow (2013). Therefore, we select the first-order nonlocal YSU and the higher-order local MYNN scheme to examine the impact of two different types of PBL schemes.

In addition, studies have suggested that less than 4 km is a reasonable choice for grid spacing to represent the convection explicitly, which means deep convection and mesoscale convective systems are assumed to be fully resolved under a fine grid size without using cumulus parameterizations (Han and Hong, 2018; Weisman et al., 1997; Willets et al., 2017; Zhang, 2019). Han and Hong (2018) found that using explicit convection (EC) in the WRF model at 3-km grid improved the heavy rainfall forecast, although suppressed the light precipitation. Meanwhile, Li and Pu (2009) suggested that using cumulus parameterization at 9-km grid may be beneficial for modelling convective systems and precipitation structures, but affected little in the simulations at 3-km grid. Therefore, we used EC as the convection treatment in high-resolution 3-km forecasts of the landed TC heavy rainfall.

The objective of this study is to investigate the key factors and physical processes regulating the distribution of heavy rainfall of landed TC Rumbia and their sensitivities to different microphysics and planetary boundary layer schemes in the convective-permitting simulations. The model differences are explored mainly from the impacts of these different physical schemes on the interaction of TC thermodynamic

structure and the environmental conditions (upper-level divergence, low-level convergence, and VWS).

The rest of the paper is organized as follows. Section 2 provides the observational data and the overview of TC Rumbia (2018), focusing on the evolution of TC intensity, track, and rainfall distributions with different synoptic weather patterns after landfall. Section 3 describes the WRF model experiments with three MPs and two PBLs both using explicit convection treatment. The results from all the sensitivity experiments and the possible physical understandings of model differences are described in Section 4 and 5, respectively. The main conclusions and discussions are summarized in Section 6.

2. Overview of Typhoon Rumbia (2018)

2.1. Track, intensity and rainfall distribution change

Fig. 1 presents the track and intensity changes of Tropical Cyclone Rumbia (2018) from 0000 UTC 16 Aug., 2018 to 1800 UTC 19 Aug., 2018 in (a), and accumulated rainfall distributions at landfall (1800 UTC 16–0600 UTC 17), inland slowing-moving (1200 UTC 17–1800 UTC 18) and recurring (0000 UTC 19–1800 UTC 19) stages in (b–d).

The observational data, here, include the best track data from Shanghai Typhoon Institute of China Meteorological Administration (STI/CMA, Ying et al., 2014; http://tcdatalyphoon.org.cn/zjljsj_sm.html), Half Hourly 0.1°x 0.1°rainfall products from the Integrated Multi-satellite Retrievals for GPM-Global Precipitation Measurement

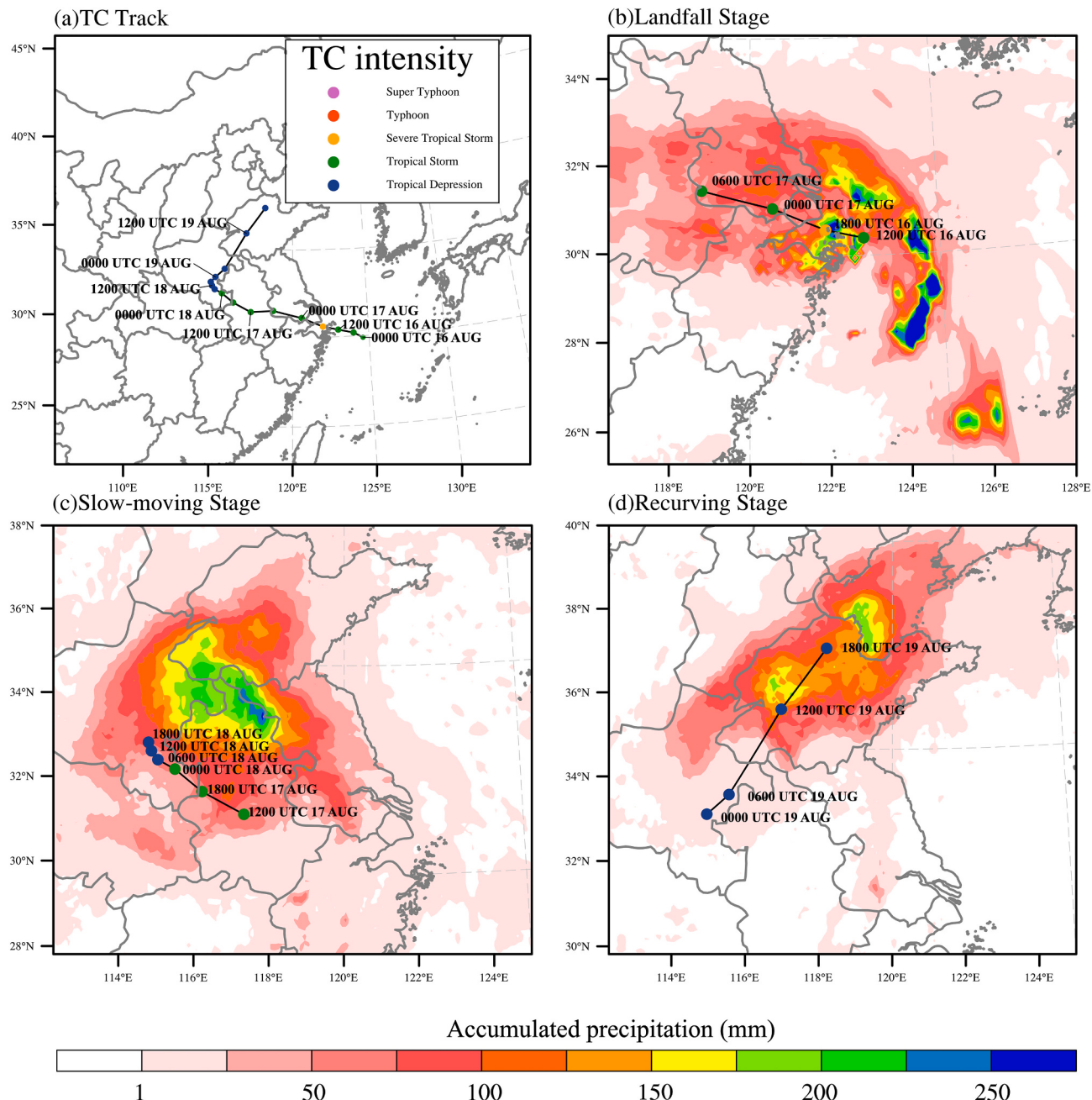


Fig. 1. (a) The track and intensity changes of Tropical Cyclone Rumbia (2018) from 0000 UTC 16 Aug., 2018 to 1800 UTC 19 Aug., 2018; (b, c, d) Accumulated rainfall (units: mm) distributions of landfall stage (1800 UTC 16–0600 UTC 17), inland slowing-moving stage (1200 UTC 17–1800 UTC 18) and recurring stage (0000 UTC 19–1800 UTC 19).

Mission (IMERG, Huffman et al., 2019; https://disc.gsfc.nasa.gov/data-sets/GPM_3IMERGHH_06/summary). TC Rumbia originated in the western North Pacific as a Tropical Storm on Aug. 15, and made landfall as a Severe Tropical Storm in Shanghai on 2000 UTC 16 Aug., 2018. Heavy rainfall was mainly concentrated near the East China Coast in the front right quadrant of the TC track (Fig. 1b). After its landfall, TC Rumbia degraded to Tropical Storm at 0000 UTC 17 Aug., moved westward and gradually slowed down. During the slow-moving stage, extensive precipitation was brought to Anhui Province, Henan Province and Shandong Province. The maximum accumulated precipitation record occurred in Anhui Province, exceeding 250 mm in 36 h. Till 1800 UTC 18 Aug., TC Rumbia began to turn northeastward in Henan Province, and persisted as a Tropical Depression but brought heavy

precipitation to Shandong Province for the next 24 h before it moved into Bohai, China.

2.2. Synoptic evolution

Fig. 2 presents synoptic patterns at 200 hPa, 500 hPa and 925 hPa as well as environmental VWS at representative time of 1800 UTC 16 in (a), 1200 UTC 17 in (b), 1800 UTC 18 in (c) and 0600 UTC 19 in (d) Aug., 2018 based on the $1^{\circ} \times 1^{\circ}$ NCEP FNL (Final) Operational Global Analysis data (<https://rda.ucar.edu/datasets/ds083.2/index.html#sf01-wl-data/ds083.2?g=22018>). The environmental VWS was defined as the wind difference between 850 hPa and 200 hPa within 800-km radius from the TC center (Feng and Shu, 2018).

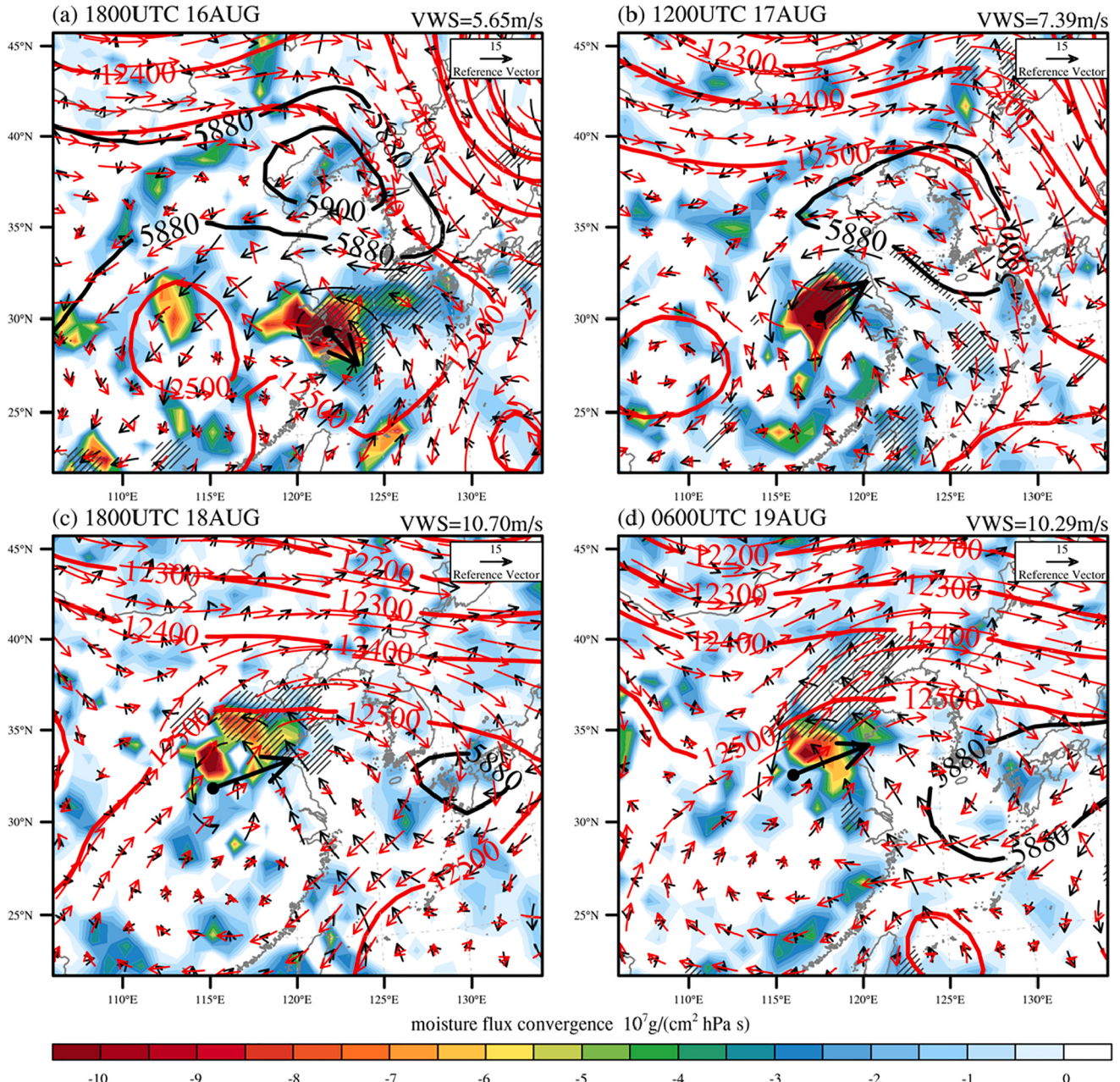


Fig. 2. Synoptic patterns at representative time of 1800 UTC 16 (a), 1200 UTC 17 (b), 1800 UTC 18 (c) and 0600 UTC 19 (d) Aug., 2018, from NCEP reanalysis data, showing geopotential height (units: gpm; red solid contours for 200 hPa, black solid contours for 500 hPa), wind field (units: $m s^{-1}$, red vectors for 200 hPa, black vectors for 925 hPa), upper-level divergence (diagonal shaded area; greater than $2.5 \cdot 10^{-5} s^{-1}$ at 200 hPa) and low-level moisture flux convergence at 925 hPa (shaded area; units: $10^7 g/(cm^2 \cdot hPa \cdot s)$). The black solid arrow indicates the vertical wind shear whose value is provided at the top-right corner of each figure. (For interpretation of the references to colour in this figure legend, the reader is referred to the web version of this article.)

During its landfall stage (Fig. 2a), TC Rumbia was located over the southern side of the strong western North Pacific Subtropical High (WNPSH), and moved to the northwest due to the strong steering flow of southeasterlies. The southerly wind was associated with the dominated South Asia High (SAH) at the upper level, leading to a weak northwesterly VWS (5.65 m/s) around the TC. The strong low-level moisture convergence area mainly occurred near the coast, corresponding to the heavy rainfall location (Fig. 1b) which may indicate the major influence of boundary frictional convergence for landfalling TCs suggested by Shapiro (1983).

At 1200 UTC 17 Aug. (Fig. 2b), the WNPSH in the north weakened and moved eastward, leading to the weakening of steering flow and slow movement of TC. During this inland slow-moving stage, the southeast outflow at the upper level and the VWS shifting to the northeast were relatively weak. The low-level moisture convergence and the upper-level divergence coexisted to the front right of the slow-moving TC track, resulting in rainfall accumulated in the VWS downshear left sector.

At 0600 UTC 10 Aug. (the recurring stage), the WNPSH stretched westward and strengthened, and the upper-level westerly jet to the north of TC circulation was enhanced, resulting in intensified environmental VWS (10.29 m/s) around TC. As such, the accompanied stronger upper-level divergence and low-level moisture convergence produced larger updrafts and thus heavier rainfall in the VWS downshear left region compared to the slow-moving stage.

3. Model experiments and evaluation methods

3.1. Model configuration and experimental design

The model used in this study is WRF version 3.9 (Skamarock et al., 2008). The computation domain is centered at (35°N, 120°E) using the Lambert Conformal map projection. It covers the East China and adjacent oceans shown in Fig. 1a at 3 km horizontal grid spacing, with total grid points of 1000 (west-east) x 900 (south-north) and refined 51 vertical levels. All model simulations included 6-h spin-up runs starting from 1800 UTC 15 Aug., 2018, with 20-s time interval, making the total integration period of 90 h till 1800 UTC 19 Aug., 2018. The initial and boundary conditions were constructed from the National Centers for Environmental Prediction (NCEP) operational global final (FNL) analyses ($1^\circ \times 1^\circ$). The NCEP ADP Global Upper Air and Surface Weather Observations (<https://rda.ucar.edu/datasets/ds337.0/>) were used for data assimilation at the initial time only via WRF three-dimensional variational data assimilation (3DVAR) system. The 30-arc sec USGS terrain data and 21-categories, 2-m resolution MODIS land use/cover data were used for static surface conditions.

Based on three MPs with two different PBLs, two groups of convection-permitting experiments were conducted to examine the sensitivity of TC Rumbia and heavy rainfall simulations to multi-physics parameterizations. Table 1 summarizes all the experimental configurations. Three MPs are Eta Ferrier (Ferrier, NOAA, 2010), WSM6 (Hong et al., 2006), and Thompson (Thompson et al., 2008) scheme. Two PBL schemes are Yonsei University (YSU, Hong et al., 2006) and Mellor-Yamada-Nakanishi-Niino level 2.5 (MYNN, Nakanishi et al., 2006) scheme. Group_MIC_YSU denotes the runs using the YSU PBL scheme

with three different MPs, and Group_MIC_MYNN only changes the PBL scheme to MYNN. Each experiment is specified hereafter by the name of its MP scheme with appended suffix of “_YSU” or “_MYNN” as the PBL scheme. For instance, Ferrier_YSU represents the experiment in Group_MIC_YSU using the Ferrier MP with the YSU PBL scheme, while Ferrier_MYNN represents that experiment in Group_MIC_MYNN using the Ferrier MP but with the MYNN PBL scheme. The other same model physics for all experiments include the Rapid Radiative Transfer Model (Mlawer et al., 1997) for longwave radiation, the Dudhia shortwave scheme (Dudhia, 1989), the Noah Land Surface Model (Tewari et al., 2004) and the Revised MM5 Monin-Obukhov scheme for surface layer (Jimenez et al., 2012).

Three MPs mainly differ in describing the categories of cloud hydrometeors and ice particle characteristics (size distribution, particle density, fallspeed), which are summarized in Table 2. The Ferrier scheme is known as the Eta grid-scale cloud and precipitation scheme released in 2001. It is a single-moment scheme that predicts the mixing ratio changes of cloud water, rain and ice. The ice here includes small ice crystals, which are dominant in cirrus and upper tropospheric ice clouds, and larger ice particles in the form of snow (aggregates), graupel (varying degrees of rimed snow), and sleet (ice pellets). The WSM6 and Thompson schemes both consider six classes of hydrometeors, including cloud water vapor, cloud water, cloud ice, rain, snow and graupel. They both assume generalized gamma distributions for all species, except that the Thompson scheme uses purely exponential distributions for snow category (Field et al., 2005). Particularly for the snow particles, the WSM6 scheme adopts spherical and constant density assumptions, but the Thompson scheme uses non-spherical assumptions for mass-size relationship (Cox, 1988), and assumes density varying inversely with the particle diameter. This leads to smaller particle sizes produced by the Thompson scheme under the same mixing ratio, which weakens the riming/deposition growth and fallspeed and thus a lower precipitation efficiency. The Thompson scheme neglects the process of cloud ice collecting rain particles due to the limited diameter of ice particles (< 200 μm), while the WSM6 scheme contains an additional growth process of graupel by collecting the cloud ice or snow and from the water vapour autoconversion.

Two PBLs mainly differ in their eddy diffusivity closure assumptions and vertical mixing processes. The YSU scheme is a non-local first-order closure which determines the vertical subgrid-scale transport based on gradient transport theory and adopts multiple vertical levels to simulate the effect of large eddies in the convective boundary layers (Hong et al., 2006). The MYNN scheme is a local higher-order scheme which determines the eddy diffusivity based on turbulent kinetic energy closure and adopts only adjacent vertical levels to estimate the turbulent fluxes through full range of atmospheric turbulent regimes (Stensrud, 2009). Meanwhile, the MYNN scheme is formulated by the thermodynamic variables that are conserved for the moist adiabatic processes, including total water mixing ratio and liquid water potential temperature, while the YSU scheme uses the potential temperature and water vapor content. More details about the differences between these two PBL schemes can also be referred to Wang et al. (2021).

3.2. Evaluation methods

To quantitatively evaluate the TC precipitation forecast skill, pattern correlation (PC, Barnston, 1992) and root mean square error (RMSE, Barnston, 1992) were used to verify the simulated spatial distribution of TC accumulated precipitation in different stages after landfall. The threat score (TS, Wilks, 2011) was specifically used to evaluate the forecast skill of heavy rainfall ($\geq 12.5 \text{ mm}/6 \text{ h}$) as a probability verification. These statistics were all calculated within 500 km distance from the TC centre. The equations of PC, RMSE and TS are as follows:

Table 1
Model physics configurations for two groups of sensitivity experiments.

Group name	Exp. name	Cloud microphysics scheme	PBL scheme
Group_MIC_YSU	Ferrier_YSU	Ferrier	YSU
	WSM6_YSU	WSM6	
	Thompson_YSU	Thompson	
Group_MIC_MYNN	Ferrier_MYNN	Ferrier	MYNN
	WSM6_MYNN	WSM6	
	Thompson_MYNN	Thompson	

Table 2

Predicted variables and key functions for microphysical particles in Ferrier, WSM6 and Thompson cloud microphysics schemes.

Cloud microphysics schemes		
Ferrier	WSM6	Thompson
Reference	NOAA, 2010	Hong and Lim, 2006
Predicted Variables	Qc Qr Qs (Qt*)	Qc Qr Qi Qs Qg
Type	Single moment	Single moment
Particle size distribution function	For precipitation ice particles: $N_x = N_0 \lambda^{-1} e^{-\lambda D_0}$	For rain, snow and graupel: $N_x(D) = N_0 e^{-\lambda_x D}$ For cloud ice: $N_i = 5.38 \times 10^7 (\rho q_i)^{0.75}$ $\rho q_i = 2.08 \times 10^{22} D_i^8$
Mass Relation	$m_i(D) = A_i D^{B_i}$ (for unrimed ice: A_i and B_i follow the table B2 from Starr and Cox (1985); for aggregates: A_i and B_i follow Locatelli and Hobbs (1974))	$m_r(D) = \frac{\pi \rho_w D^3}{6}$ $m_i(D) =$ $\left(\frac{2.08 \times 10^{22}}{8.38 \times 10^{30}} \right)^{0.25} D^2$ $m_s(D) = \frac{\pi \rho_s D^3}{6}$ $m_g(D) = \frac{\pi \rho_g D^3}{6}$
Terminal Velocity	$V_i(D) = A_i D^{B_i}$	$V_x = a_x D_x^{b_x} \left(\frac{1.28}{\rho} \right)^{0.5}$ $a_r = 84.19, b_r = 0.80$ $a_s = 11.72, b_s = 0.41$ $a_g = 330.00, b_g = 0.80$
Particle Density	ρ_i depends on the formation process.	$\rho_s = 100$ $\rho_g = 500$
Description Of Special Variables	Subscript 't' denotes total concentration. The Ferrier predicts only total condensate, which is the sum of cloud water, rain, and ice.	Subscript 't' denotes 'r', 's' and 'g'. a and b are mass power-law constants
		$\rho_i = 890$ $\rho_s = 0.13 D^{-1}$ $\rho_g = 500$ $\kappa_0, \kappa_1, \Lambda_0, \Lambda_1$ and μ_s are constants. a and b are mass power-law constants f is velocity power-law constant.

General variables: Subscript 'c' denotes cloud water. Subscript 'r' denotes rain water. Subscript 'i' denotes cloud ice. Subscript 's' denotes snow. Subscript 'g' denotes graupel. Subscript 'w' denotes water. 'Q' and 'q' denote mixing ratio. 'N' denotes number concentration. 'D' denotes diameter of the particle. 'V' denotes terminal velocity. 'm' denotes mass. 'λ' denotes slope parameter. ' N_0 ' denotes intercept parameter. 'μ' denotes the shape parameter. ρ denotes air density.

$$PC(F, O) = \frac{\sum_{i=1}^n (F_i - \bar{F})(O_i - \bar{O})}{\sqrt{\sum_{i=1}^n (F_i - \bar{F})^2 \sum_{i=1}^n (O_i - \bar{O})^2}} \quad (1)$$

$$RMSE(F, O) = \sqrt{\frac{1}{N} \sum_{i=1}^N (F_i - O_i)^2} \quad (2)$$

$$TS = \frac{a}{a + b + c} \quad (3)$$

where "F", "O", and "N" denote forecast, observation, and total number of the grids, respectively. "a" is the number of correct forecasts of events occurring (hits), "b" is the number of events observed but not forecasted (misses), "c" is the number of events forecasted but not observed (false alarms). TS measures the fraction of observed and/or forecast events that were correctly predicted for a given precipitation threshold.

In addition to the standard verification methods above, we used the Structure-Amplitude-Location (SAL) technique (Wernli et al., 2008) to further quantify the TC heavy precipitation forecast at critical moments in the three stages. SAL is an object-based method which quantifies the precipitation forecast from three key aspects: structure (S), amplitude

(A), and location (L). The precipitation field (R) represents every grid point where it rained. The observed (R_{obs}) and model precipitation fields (R_{mod}) are classified into different precipitation objects (R_n) according to a threshold contour (R^*). Starting from the grid points with local maximum exceeding the threshold value R^* , the adjacent grids should be contained in the same object as long as the grid point value $R_{i,j}$ is greater than R^* . The objects are denoted as R_n , $n = 1, \dots, M$, where M corresponds to the total number of objects in the domain for verification. In this study, R^* was taken as 12.5 mm/6 h to be comparable with TS values.

The amplitude component (A) measures the relative bias of model simulated rainfall averages in precipitation field. It is calculated as follows:

$$A = \frac{D(R_{mod}) - D(R_{obs})}{0.5 \times [D(R_{mod}) + D(R_{obs})]} \quad (4)$$

$$D(R) = \frac{1}{N} \times \sum_{(i,j) \in D} R_{i,j}$$

where R_{mod} (R_{obs}) denotes the precipitation data from the model output (observation). N is the number of grid points in domain. $D(R)$ denotes

the average precipitation of all grid points in R (the whole domain). A > 0 (< 0) indicates an overestimation (underestimation) of model precipitation.

The location component (L) quantifies the biases of precipitation location in two aspects, including the deviation of model simulated precipitation field's center of mass against the observation (L_1), and the deviation of individual precipitation objects of interested from the total field's center of mass(L_2). The equations are as below.

$$L = L_1 + L_2 \quad (5)$$

$$L_1 = \frac{|x(R_{mod}) - x(R_{obs})|}{d}$$

$$L_2 = \frac{2 \times |r(R_{mod}) - r(R_{obs})|}{d}$$

$$r = \frac{\sum_{n=1}^M R_n |x - x_n|}{\sum_{n=1}^M R_n}$$

$x(R_{mod})$ and $x(R_{obs})$ denote the center of mass of the precipitation objects R_n in R_{mod} and R_{obs} respectively. r denotes the weighted average distance between the centers of mass of the individual objects (x_n) and the center of mass of the total precipitation field (x). L ranges in [0,2], and the larger the value of L, the greater the deviation of model precipitation location.

The structure component (S) measures the biases of normalized distribution of model simulated precipitation of all grid points in individual precipitation objects compared to the observations, which captures information about the size and shape of precipitation objects.

$$S = \frac{V(R_{mod}) - V(R_{obs})}{0.5 \times [V(R_{mod}) + V(R_{obs})]} \quad (6)$$

$$V(R) = \frac{\sum_{n=1}^M R_n V_n}{\sum_{n=1}^M R_n}$$

$$V_n = \sum_{(i,j) \in R_n} \frac{R(i,j)}{R_n^{max}} = \frac{R_n}{R_n^{max}}$$

V_n denotes a “scaled volume” of the n th object (R_n) and R_n^{max} denotes the maximum precipitation value in the object. $V(R_{mod})$ and $V(R_{obs})$ calculate the weighted mean of all precipitation objects' scaled volume from model simulations and observations, respectively. $S > 0$ ($S < 0$) indicates that modelled precipitation objects are generally too widespread in covered area and/or their normalized distributions are too flat (too small and/or too peaked).

4. Model sensitivities to different physical parameterizations

4.1. TC intensity and track

Fig. 3a presents the evolution of simulated track bias from all two groups of experiments from 0000 UTC 16 Aug. to 1800 UTC 19 Aug. for TC Rumbia. All the simulated track biases generally increased with the forecast time. Among three MPs, the Ferrier scheme tended to produce the largest track bias especially at the two inland stages. Among two PBL schemes, the YSU scheme performed better as the forecast time increased. Fig. 3b and c compare the evolution of observed and simulated TC intensity in terms of minimum sea level pressure (MSLP) and maximum wind speed (MWS). Since the observed wind speed was derived from a 2-min average and the model output was instantaneous values, thus there may exist computation discrepancy. All experiments generally reproduced the entire evolution of TC MSLP and MWS, including the intensification at 1800 UTC 16 before landfall and the slow weakening and maintenance after landfall. However, the use of the

MYNN PBL scheme for all three MPs systematically produced higher MSLP and lower MWP than the use of YSU PBL scheme throughout the whole landfalling stage.

During the landfall stage, both groups of experiments underestimated the TC center pressure intensity, but Group_MIC_YSU generally had lower biases in both MSLP and MWS. Similar results showing the advantage of using the YSU scheme could also be found in Zhu et al. (2014) and Rajeswari et al. (2020). Among these three MPs in Group_MIC_YSU, the Ferrier scheme produced the strongest TC which was closest to the observed MSLP, and the simulated MWS was also the largest, even exceeding the observation. However, at the two inland stages, the Ferrier scheme in both groups of experiments produced weaker TC than the other two MPs, and the Ferrier scheme with the use of the MYNN PBL scheme produced the largest underestimation errors of TC intensity, while the WSM6 and Thompson MP schemes with the use of the YSU PBL scheme better reproduced the TC intensity in terms of both MSLP and MWS.

4.2. TC induced heavy rainfall

This section quantifies the model's simulation of the distribution of total accumulated rainfall associated with TC Rumbia during three different stages using PC and RMSE, with the focus on the forecast skill of heavy rainfall (6-h accumulation ≥ 12.5 mm) using the TS scores and SAL technique.

Table 3 summarizes the PC and RMSE values for the accumulated rainfall as well as the TS scores for heavy rainfall at three stages for both groups. At the landfall stage, the Ferrier MP scheme in both groups showed consistent advantages over the other two MPs in forecasting the accumulated rainfall distribution and heavy rainfall intensity with higher PC, TS and lower RMSE. Meanwhile, Ferrier YSU had higher forecast skill in heavy rainfall intensity with a larger TS value than Ferrier_MYNN.

However, at the two inland stages, the WSM6 and Thompson MP schemes both outperformed the Ferrier MP scheme in either group of experiments in forecasting the accumulated rainfall distribution and heavy rainfall intensity. In particular, WSM6_YSU showed the best performance with the highest PC, TS and the lowest RMSE at the slow moving stage, and Thompson_YSU showed significant advantages with the highest values of PC, TS and the lowest value of RMSE.

Fig. 4 further compares the changes of TS scores for 6-hourly TC induced heavy rainfall simulations with the increase of forecast time after TC Rumbia landed. At the landfall stage, the Ferrier_YSU began to show advantages after 24-h forecast, and WSM6_YSU and Thompson_YSU consistently outperformed others at the two inland stages, showing relatively stable forecast skills for heavy rainfall with TS scores of about 0.5. The main difference is that the WSM6 MP scheme showed higher TS scores over the entire slow-moving stage after 36-h forecast, but the Thompson MP scheme began to show superiority over others after 78-h forecast at the recurving stage.

Fig. 5 compares the geographic distributions of 6-h accumulated rainfall induced by TC Rumbia at 1800 UTC 16 Aug., 2018 during the landfall stage from the IMERG observed precipitation data and two groups of model simulations as well as their biases. We define the area within (beyond) a radius of 100 km as the inner (outer) core region according to the distribution of observed maximum wind speed (not shown here), and the spiral rain band between 100 and 250 km and beyond 250 km as the inner and outer spiral rain band, respectively, followed Chen et al. (2018). All experiments generally reproduced the location of TC center and the northwesterly VWS with slightly overestimated magnitude, and well captured the main rain bands in the front right quadrant of TC track, except that the outer spiral rain band beyond 250 km and the coastal rain in the inner core region were underestimated. In particular, the use of the YSU PBL scheme for all three MPs generally produced smaller underestimation biases of coastal rain in the TC inner core than the use of MYNN PBL scheme. In Group_MIC_YSU, the

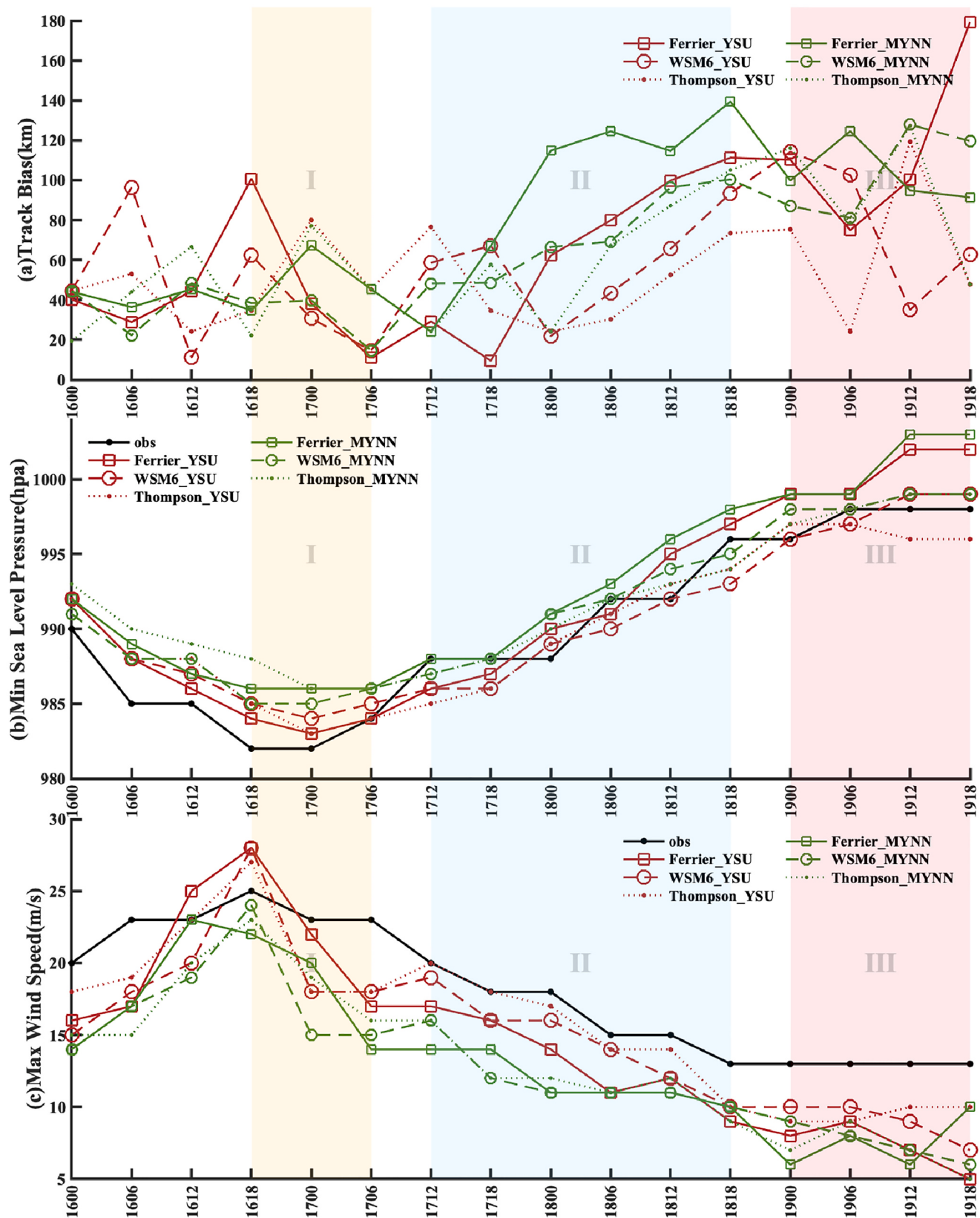


Fig. 3. Time series of (a) simulated track bias, (b) observed and simulated minimum sea level pressure (hPa) and (c) maximum wind speed (m s^{-1}) from the simulations of two groups and the CMA best-track data during 0000 UTC 16 Aug-1800 UTC 19 Aug.

Table 3

Threat scores (TS) for heavy rainfall (6-h accumulation ≥ 12.5 mm), pattern correlations (PC) and root-mean-square error (RMSE) at different stages.

Group name	Exp name	1618–1706 (Landfall)			1712–1818 (Slow-moving)			1900–1918 (Recurving)		
		TS (≥ 12.5 mm)	PC	RMSE	TS (≥ 12.5 mm)	PC	RMSE	TS (≥ 12.5 mm)	PC	RMSE
Group_MIC_YSU	Ferrier_YSU	0.54	0.68	19.36	0.39	0.72	20.46	0.14	0.47	17.86
	WSM6_YSU	0.49	0.65	19.92	0.60	0.86	16.72	0.38	0.70	14.63
	Thompson_YSU	0.53	0.63	20.20	0.56	0.82	17.61	0.59	0.79	12.79
Group_MIC_MYNN	Ferrier_MYNN	0.50	0.70	18.94	0.33	0.65	22.60	0.12	0.36	19.48
	WSM6_MYNN	0.43	0.62	20.43	0.41	0.76	19.01	0.24	0.57	16.68
	Thompson_MYNN	0.42	0.64	20.11	0.57	0.80	17.57	0.29	0.56	17.28

Dates as 1800 UTC 16 are abbreviated with the format like “1618”. The bold data denote the groups with best performance in each stage.

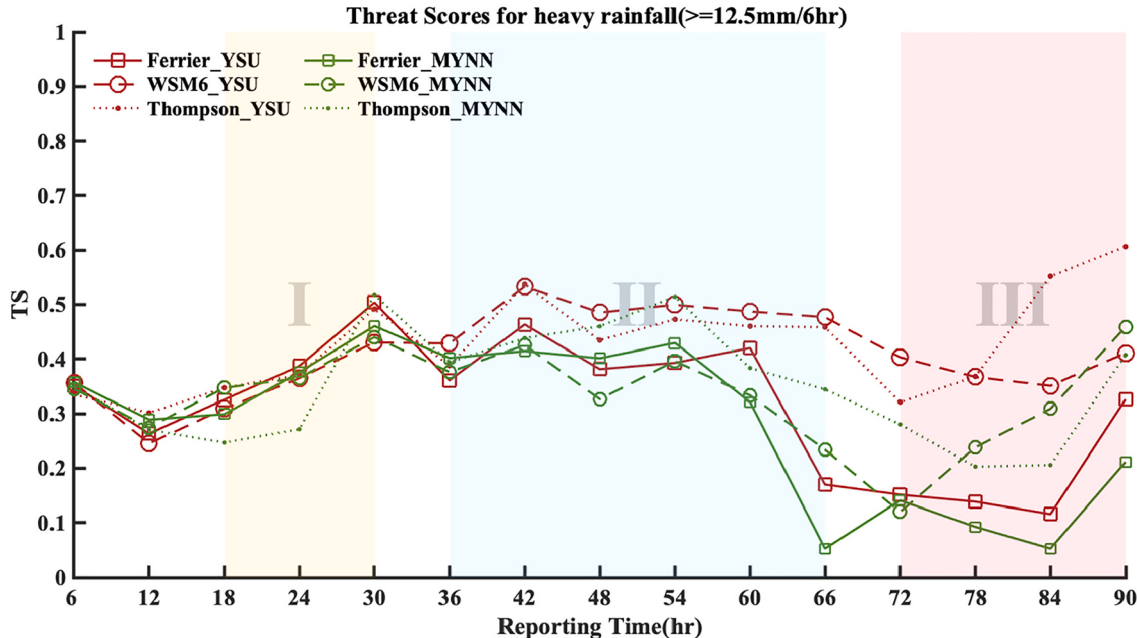


Fig. 4. Time series of threat scores (TS) for heavy rainfall (simulated accumulated precipitation for every 6-h period in each grid greater than 12.5 mm) from the simulations of two groups during 0600 UTC 16 Aug.–1800 UTC 19 Aug.

WSM6 and Thompson MP schemes both largely overestimated the environmental VWS and the intensity of inner rain band, while the Ferrier MP scheme produced the smallest VWS and rainfall bias within 250 km, albeit with a more scattered and widespread rainfall area.

As shown by the SAL values for 1800 UTC 16 Aug. in Fig. 8, three MPs in Group_MIC_YSU all produced positive S and negative A, indicating the scattered distribution of heavy rainfall with underestimated intensity. Among them, the Ferrier_YSU showed advantages over the others in capturing the amplitude of rainfall (A) with the least underestimation at this time, albeit with larger biases in structure (S) and location (L) which were also identified in Fig. 5. Compared to Group_MIC_YSU, the use of MYNN PBL scheme mainly affected the performance of Ferrier and Thompson MP scheme, by further reducing the amplitude of heavy rainfall but improving the structure and location.

Figs. 6 and 7 compare the geographic distributions of 6-h accumulated rainfall associated with TC Rumbia during the two inland stages from the observation and two groups of experiments as well as the model biases at 1200 UTC 18 and 1200 UTC 19 Aug. respectively. At both stages, the Ferrier MP scheme showed larger biases than the other two MPs in simulating the TC center location and the environmental VWS. This is consistent with the above analyses that the Ferrier MP scheme produced systematically larger TC track errors in these two stages. The heavy rainfall distributions simulated by the Ferrier MP scheme were also worse than the other two MPs.

Particularly at the slow-moving stage, all experiments well captured the general pattern of heavy rainfall in the downshear left region, but the

simulated rainfall areas were too tight towards the TC inner core, leading to the overestimated rainfall around the inner core but large underestimation in the outer core region. On the other hand, compared to Group_MIC_YSU, Group_MIC_MYNN produced weaker rainfall in the outer rainband but stronger rainfall in the inner core with weaker VWS.

The SAL values for 1200 UTC 18 in Fig. 8 more clearly showed that at the slow-moving stage, all experiments produced negative S and A, and the Ferrier MP scheme in either group systematically produced larger L than the other two MPs. Specifically, in Group_MIC_YSU, the WSM6 and Thompson MP schemes both outperformed the Ferrier MP scheme in forecasting the total rainfall amplitude and heavy rainfall location and structure. However, the use of MYNN PBL degraded the skill of Group_MIC_YSU in forecasting heavy rainfall location for all three MPs with larger L, and significantly increased the biases of heavy rainfall amplitude and structure for the WSM6 scheme. Therefore, WSM6_YSU outperformed others in heavy rainfall forecast at this slow-moving stage with the smallest biases in SAL values.

As shown by the SAL values for 1200 UTC 19 Aug. in Fig. 8, at the recurving stage, the WSM6 and Thompson MP schemes in either group consistently showed superiority in capturing heavy rainfall structure and location with significantly lower biases than the Ferrier MP scheme. Compared to the use of the YSU PBL scheme, the use of MYNN PBL scheme systematically reduced the heavy rainfall amplitude for all three MPs, and increased the biases in heavy rainfall structure and location for the Ferrier and Thompson MP schemes. Therefore, Thompson_YSU is superior in heavy rainfall forecast at this inland recurring stage, which is

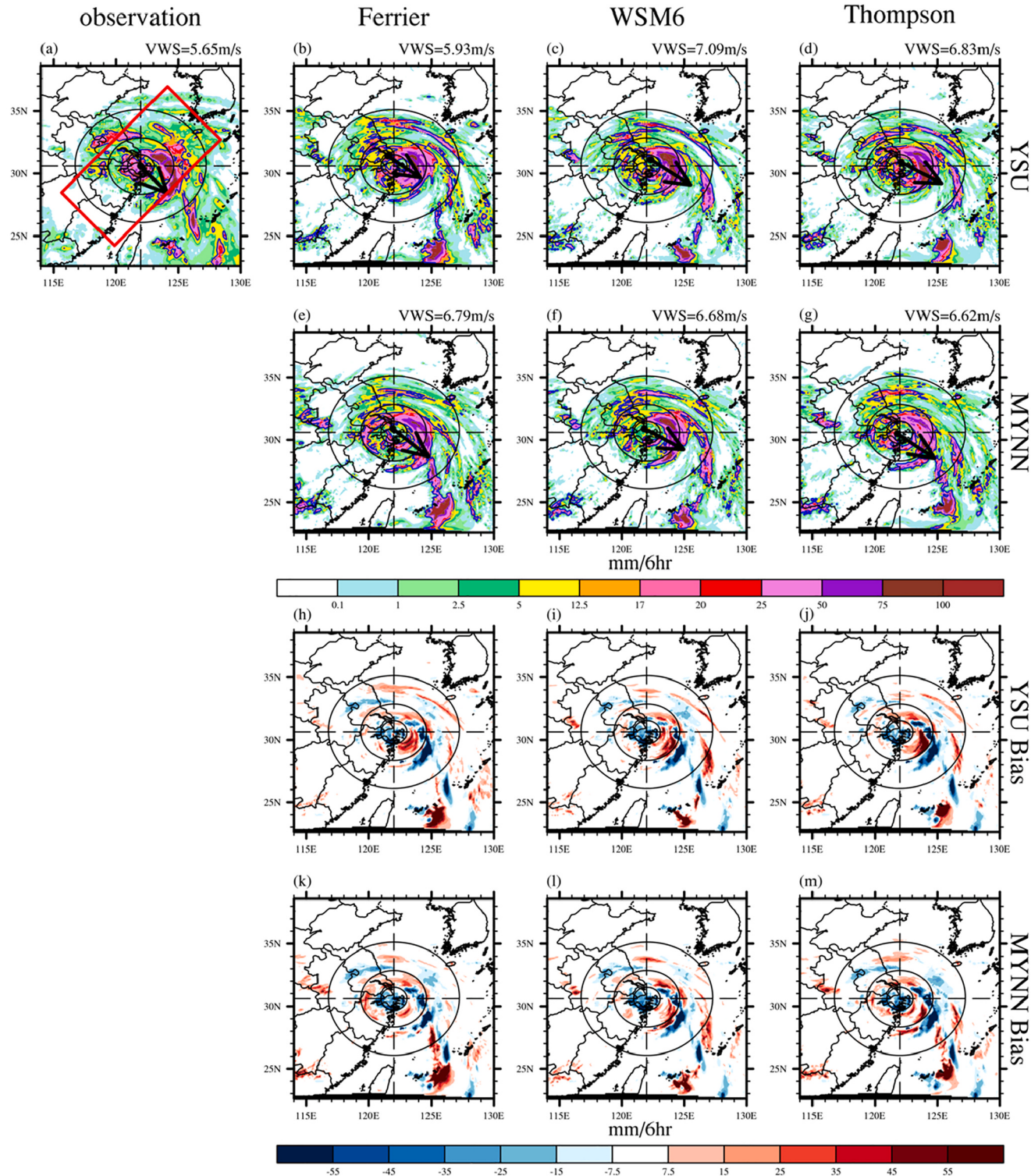


Fig. 5. The geographic distributions (a-g) of 6-h accumulated rainfall (units: mm) of TC Rumbia (2018) at landfall (1800 UTC 16 Aug., 2018) from two groups of model experiments (Group_MIC_YSU and Group_MIC_MYNN) and their simulated biases (h-m) compared to the IMERG observation. The blue solid contour denotes the accumulated rainfall greater than 12.5 mm/6 h. The intersection of the two dash lines is the center of the observation TC center. Three concentric circles denote 100 km, 250 km and 500 km distance from the TC center. The black dot denotes the simulated TC center and the black solid arrow denotes the environmental vertical wind shear. The red rectangle denotes the cross section area for Figs. 10 and 15. (For interpretation of the references to colour in this figure legend, the reader is referred to the web version of this article.)

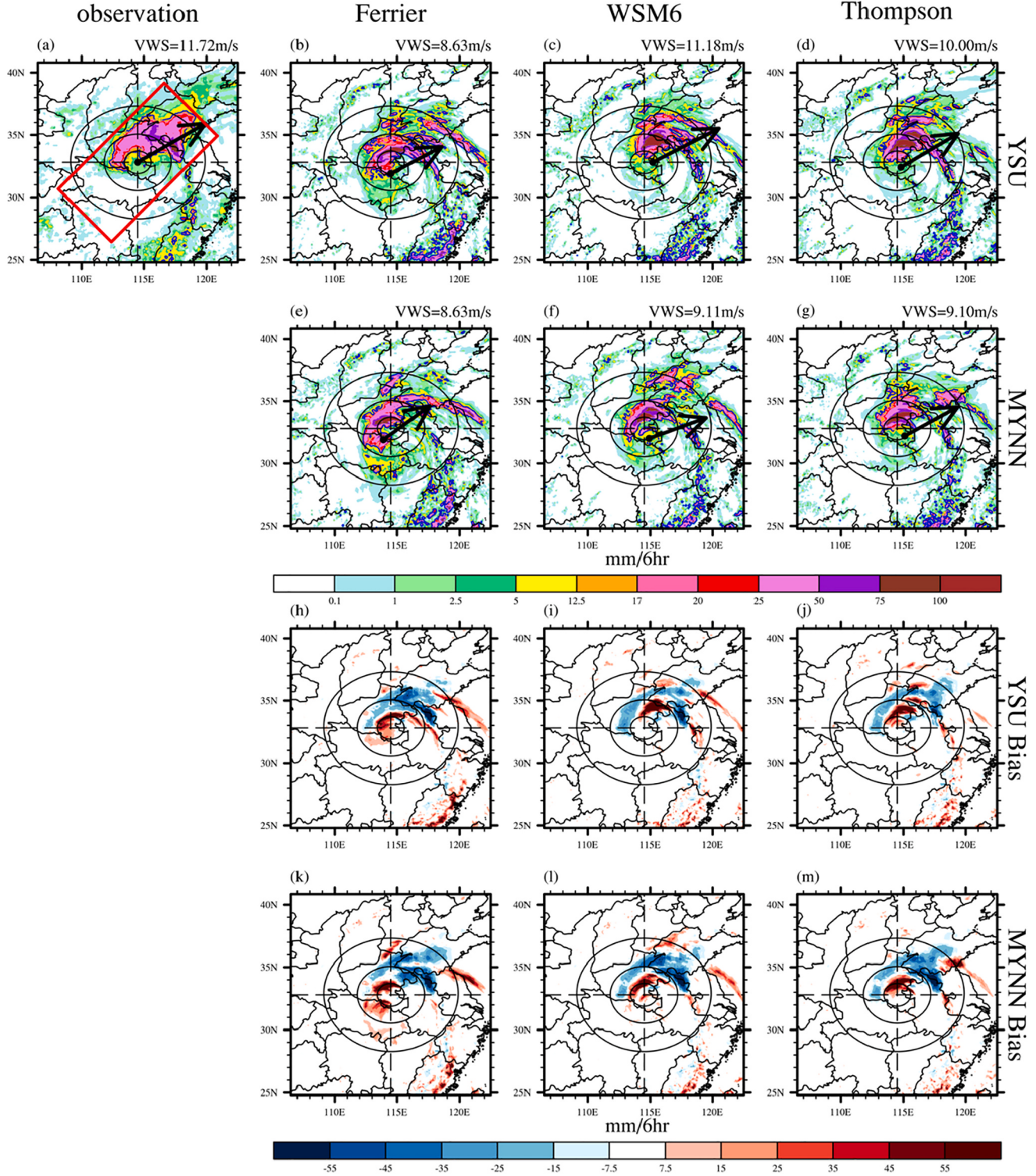


Fig. 6. Same as Fig. 5 but for slow-moving stage (1200 UTC 18 Aug., 2018).

shown by its smallest biases of heavy rainfall structure (S), location (L) and slightly overestimated intensity (A).

Overall, it is clear that more advantages were gained in the forecast of three-stages TC-induced heavy rainfall by using the YSU PBL scheme compared to the MYNN PBL scheme. With the use of the advantageous YSU PBL scheme, the Ferrier MP scheme at the landfall stage showed advantages over the other two MPs in simulating the TC intensity with the smallest underestimation, and better captured the accumulated

rainfall distribution and heavy rainfall intensity, but with a scattered structure. However, at the two inland stages, the WSM6 and Thompson MP schemes better reproduced the TC intensity with slight overestimation, and showed their respective advantages in forecasting the accumulated rainfall distribution and heavy rainfall location and structure.

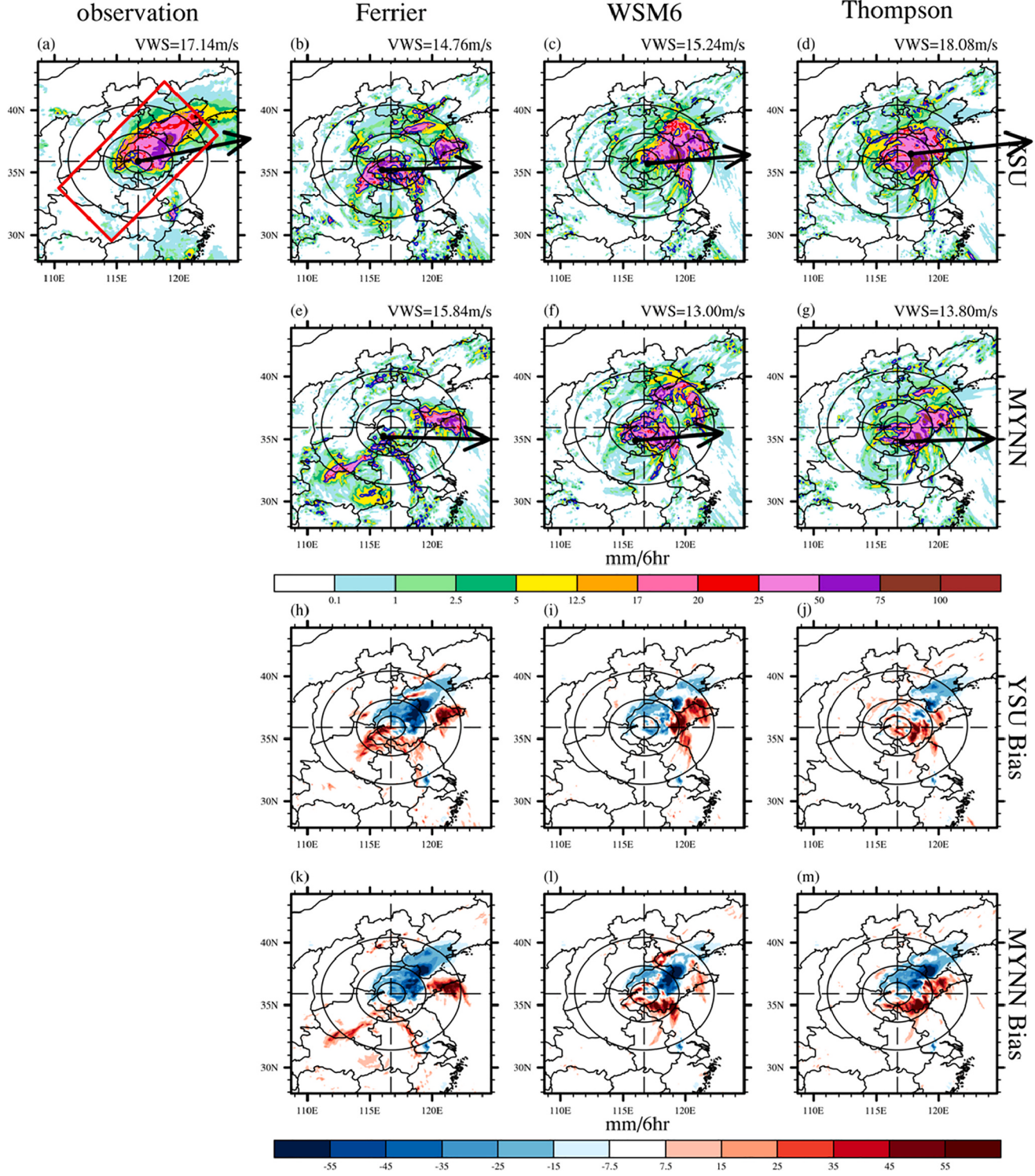


Fig. 7. Same as Fig. 5 but for recurring stage (1200 UTC 19 Aug., 2018).

5. Possible understanding of forecast skill dependence

In the following section, two aspects will be focused: 1) How do three different MP schemes affect the simulations of thermodynamic structures of TC Rumbia and associated heavy rainfall at different stages after landfall? 2) Why does the use of the MYNN PBL scheme systematically produce weaker TC intensity and precipitation than the use of the YSU PBL scheme for all three MPs at different stages?

5.1. Microphysics parameterization impacts

5.1.1. TC thermodynamic structures

Fig. 9 compares the time-height distributions of simulated mixing ratios of five types of cloud hydrometeors (cloud water, rain, cloud ice, snow, and graupel) averaged within the radius of 500 km from TC center in Group_MIC_YSU. Three MPs primarily differed in the simulations of ice-phased hydrometeors in the upper troposphere (500 hPa - 200 hPa), which is mainly related to their different treatment of ice particles. The

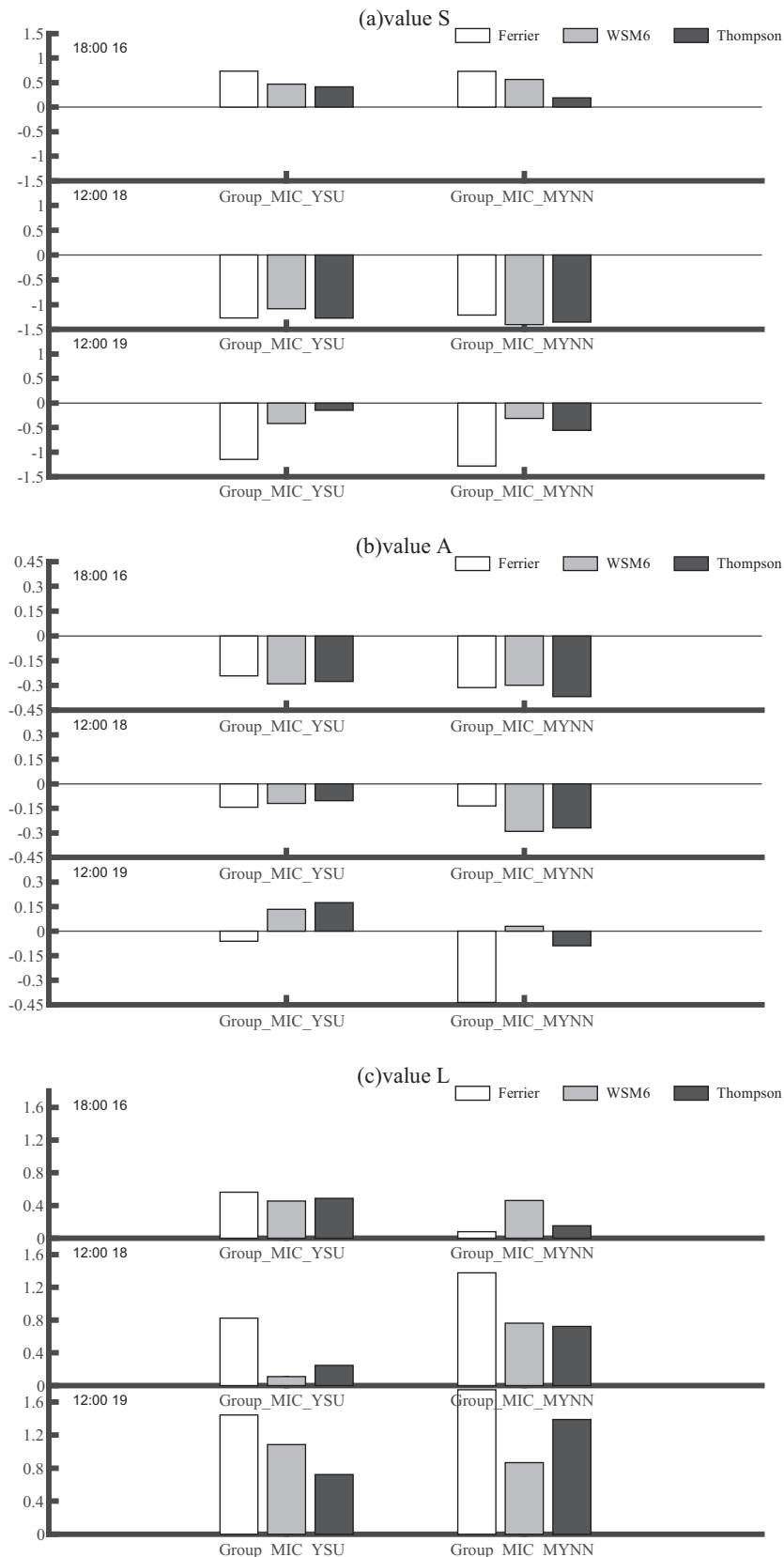


Fig. 8. SAL evaluation. The threshold was set for heavy rainfall ($\geq 12.5 \text{ mm/6 h}$) distributions at landfall (1800 UTC 16 Aug., 2018), slow-moving stage (1200 UTC 18 Aug., 2018) and recurving stage (1200 UTC 19 Aug., 2018) in 500 km distance from TC center.

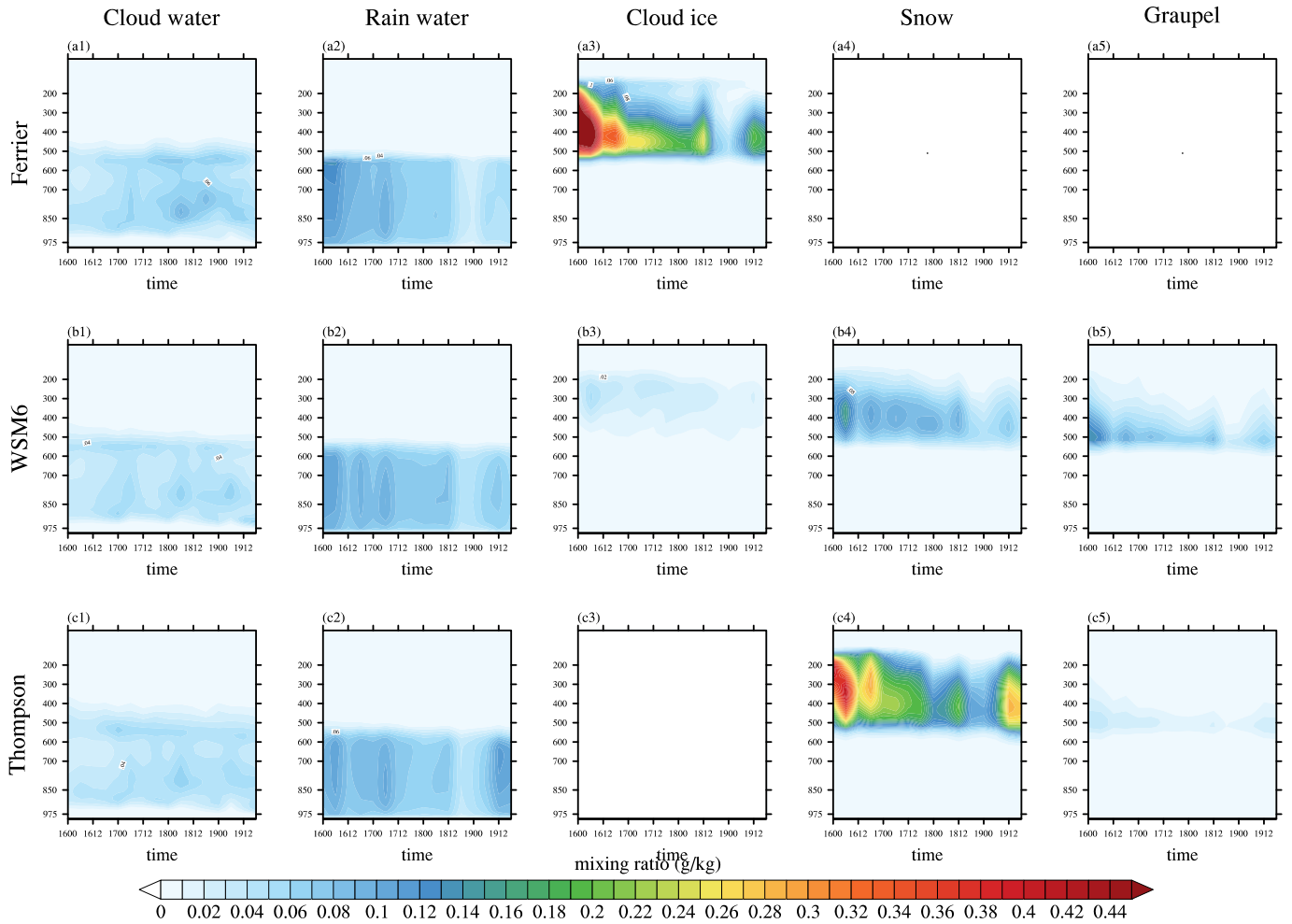


Fig. 9. Time-height distributions of the mixing ratio (units: g kg^{-1}) of cloud hydrometeors (averaged within 500 km radius from the storm center) in Group_MIC_YSU run using three different MP schemes during 0000 UTC 16 to 1800 UTC 19 Aug.

Ferrier MP scheme only predicts one type of ice-phased particle by treating all the small ice crystals and large precipitating ice as total ice particles (shown in Table 2), which led to the highest mixing ratio of cloud ice gathered at the landfall stage. On the other hand, the WSM6 and Thompson MP schemes both predict three types of ice-phased particles but with different assumptions. Specifically, the WSM6 MP scheme produced the highest mixing ratio of graupel due to two main reasons: 1) it assumes spherical and constant density for ice particles, which leads to more particles of large radii; 2) it includes additional growth process of graupel by collecting the cloud ice or snow and from the water vapour autoconversion (Hong et al., 2006). However, the Thompson MP scheme produced more snow, less graupel but too little cloud ice. Because it adopts the number concentration assumption of Field et al. (2005) which tends to generate more small snow particles, and the ice particles with radii greater than $200 \mu\text{m}$ are all converted to snow particles (Thompson et al., 2008). The formation of different ice-phased particles in the upper levels not only produced strong diabatic heating due to the conversion from cloud ice, water to graupel or snow, which enhanced the updrafts and TC intensity, but also produced stronger cooling effect from the associated melting processes in the downdrafts, which reduced the updrafts and TC intensity (Lord and Lord, 1988). Therefore, such different distributions of ice-phased particles and associated diabatic heating process among three MPs can directly affect the strength of updrafts and the associated TC circulation, which contributed to the differences in the simulated TC intensity and heavy rainfall. This will be shown as follows.

Fig. 10 presents the distance-height cross sections of southwest-

northeast averaged equivalent potential temperature, zonal-vertical wind and microphysical heating rate along the red rectangles (Figs. 5a, 6a, 7a) from Group_MIC_YSU. Previous studies have suggested that diabatic heating at different radial locations affects the TC structure and intensity in different ways. For instance, the diabatic heating in the eyewall tends to accelerate the development of secondary circulation in the inner core and thus intensifies the TC fastly (Chen et al., 2018). On the other hand, the diabatic heating in the inner spiral rainband mainly contributes to the enhancement of TC intensity (Li et al., 2014), but it is opposite to the effects of the diabatic heating in the outer spiral rainbands where heating is detrimental to TC intensification (Wang, 2009). As such, the differences in simulated TC structure and intensity by three MPs are explained as below.

At the landfall stage (1800 UTC 16 Aug.), the WSM6 and Thompson MP schemes both produced stronger diabatic heating near the eyewall ($\sim 100 \text{ km}$) due to the conversion from cloud ice and water to graupel or snow in the upper levels, leading to stronger updrafts and associated secondary circulations which was supposed to increase the TC intensity. However, these two schemes both produced stronger diabatic heating processes in the outer spiral rain band ($\sim 500 \text{ km}$) which inhibited the TC intensification. Meanwhile, they produced diabatic cooling outside the eyewall due to evaporation of cloud droplets and rainwater, melting of snow and graupel, and sublimation of snow and cloud ice, which reduced the updrafts and TC intensity. Therefore, the combined effects from these diabatic processes led to weaker TC intensity produced by the WSM6 and Thompson schemes compared to the Ferrier scheme. However, the Ferrier scheme tended to have stronger upper-level warm core,

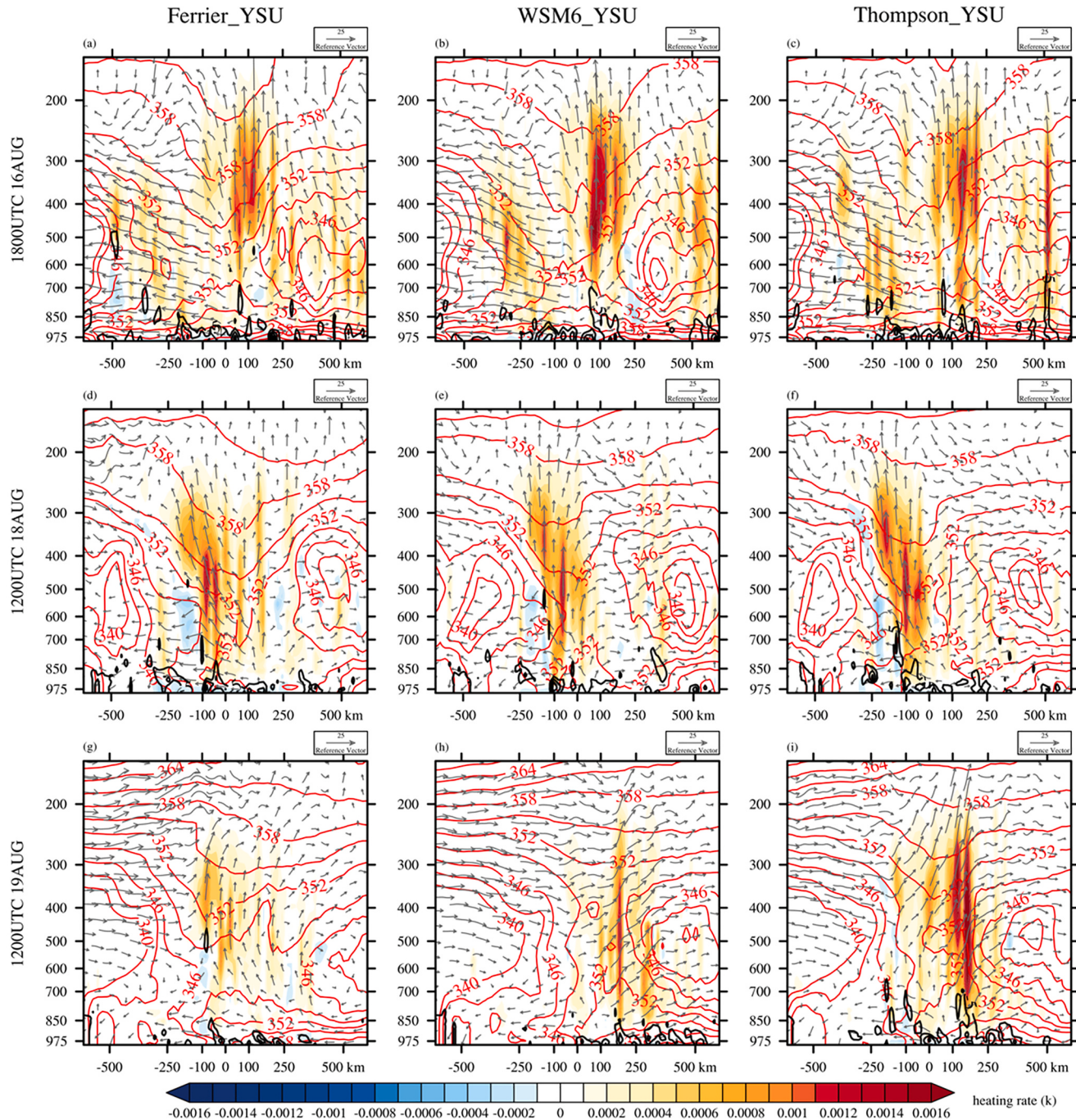


Fig. 10. Distance-height cross sections of southeast-northwest averaged equivalent potential temperature (units: K; red solid contours), wind field (units: m s^{-1} ; vectors; vertical velocity magnified 100 times to adapt zonal wind), moisture flux divergence (units: $10^7 \text{ g}/(\text{cm}^2 \cdot \text{hPa} \cdot \text{s})$; black contours) and microphysical heating rate (units: k; shaded area) for the same region of the red rectangle in Figs. 5–7a at three representative time in Group_MIC_YSU using three MP schemes. The horizontal axis denotes distance from the observed TC center. (For interpretation of the references to colour in this figure legend, the reader is referred to the web version of this article.)

which is mainly caused by the diabatic heating due to the formation of a large amount of cloud ice particles.

At the slow-moving stage (1200 UTC 18 Aug.), with the intensified upper-level westerly wind, the WSM6 and Thompson schemes simulated a more asymmetrical structure with stronger updraft and diabatic heating in the inner core and inner spiral rain band. The stronger updrafts were promoted to a higher level where the outflow could better coordinate with the upper westerlies and brought the upper-level ice-phased particles to a scattered field. Though the Ferrier scheme still maintained a strong warm core with a larger amount of cloud ice, it

produced stronger diabatic cooling outside the eyewall due to evaporation of cloud droplets or rainwater and melting of ice particles, which reduced the horizontal gradient of equivalent potential temperature and TC intensity.

At the recurving stage (1200 UTC 19 Aug.), the WSM6 scheme produced stronger diabatic heating and overestimated rainfall center in the outer rain band ($\sim 500 \text{ km}$), while the Ferrier scheme only produced diabatic heating and rainfall with underestimated rainfall bias in the inner core ($\sim 100 \text{ km}$). However, the Thompson scheme produced a more frontlike zone outside the eyewall on the downshear side, and

generated stronger diabatic heating, upper-level outflows and TC updrafts within the inner rain band (~ 250 km), leading to its superiority in simulating stronger TC intensity and heavy rainfall especially in the inner rain band.

The relationship between the simulation of intensity of TC and its associated rainfall at different landfalling stages was further examined. Fig. 11 presents the time evolution of observed TC intensity in terms of the minimum sea level pressure and accumulated rainfall in 500-km radius around the TC center, as well as the respective model biases from Group_MIC_YSU. Yu et al. (2017) suggested that the rainfall rate and type in different radii of TCs shows different relationship with TC intensity, such as rainfall in the inner core dominated by strong convective precipitation is generally correlated with increasing TC intensity, but the rainfall beyond the outer core region with large stratiform and sparse convective precipitation is insensitive to the change of TC intensity (Hence and Houze, 2012). This is also evident in this case.

At the landfall stage when rainfall mainly occurred in inner core and inner rainband, the observed rainfall rapidly increased with the intensified TC. All three MP schemes largely underestimated the TC intensity, which was highly consistent with the underestimation of TC rainfall. Among them, the Ferrier MP scheme produced the TC intensity closest to the observation, corresponding to its relatively smallest rainfall bias. At the slow-moving stage when rainfall mainly occurred in outer rainband, the observed TC intensity gradually weakened, but the rainfall continued increasing. Till the recurving stage when Rumbia was mainly

controlled by the upper-level westerly jet, the TC intensity continued to weaken, but the observed rainfall sharply increased. Although the simulated TC intensity by the WSM6 and Thompson schemes was generally stronger than the observation, the rainfall intensity was still systematically underestimated. This suggests that the intensity of rainfall concentrated in the inner core at the landfall stage was more regulated by the TC intensity, compared to the intensity of rainfall located in the outer core region as TC moved inland.

5.1.2. Environmental factors

As suggested by Feng and Shu (2018), environmental factors, such as VWS, upper-level divergence, and low-level moisture convergence, are the key factors affecting the heavy rainfall induced by weak landfalling TCs. Fig. 12 compares the geographic distributions of 200-hPa wind divergence, 925-hPa moisture flux divergence and surface heavy rainfall (≥ 12.5 mm/6 h) along with environmental VWS between the observations and the Group_MIC_YSU simulations at three stages. As the TC Rumbia continued to move inland, the observed environmental VWS was increasing from 5.65 m/s at the landfall stage to 11.72 m/s at the slow-moving stage, and eventually reached 17.14 m/s at the recurving stage. The structure and location of heavy rainfall in observations largely depended on the environmental VWS and the coverage of upper-level wind divergence and low-level moisture convergence.

In Group_MIC_YSU, three MPs mainly differed in the simulations of the upper-level wind divergence and the low-level moisture

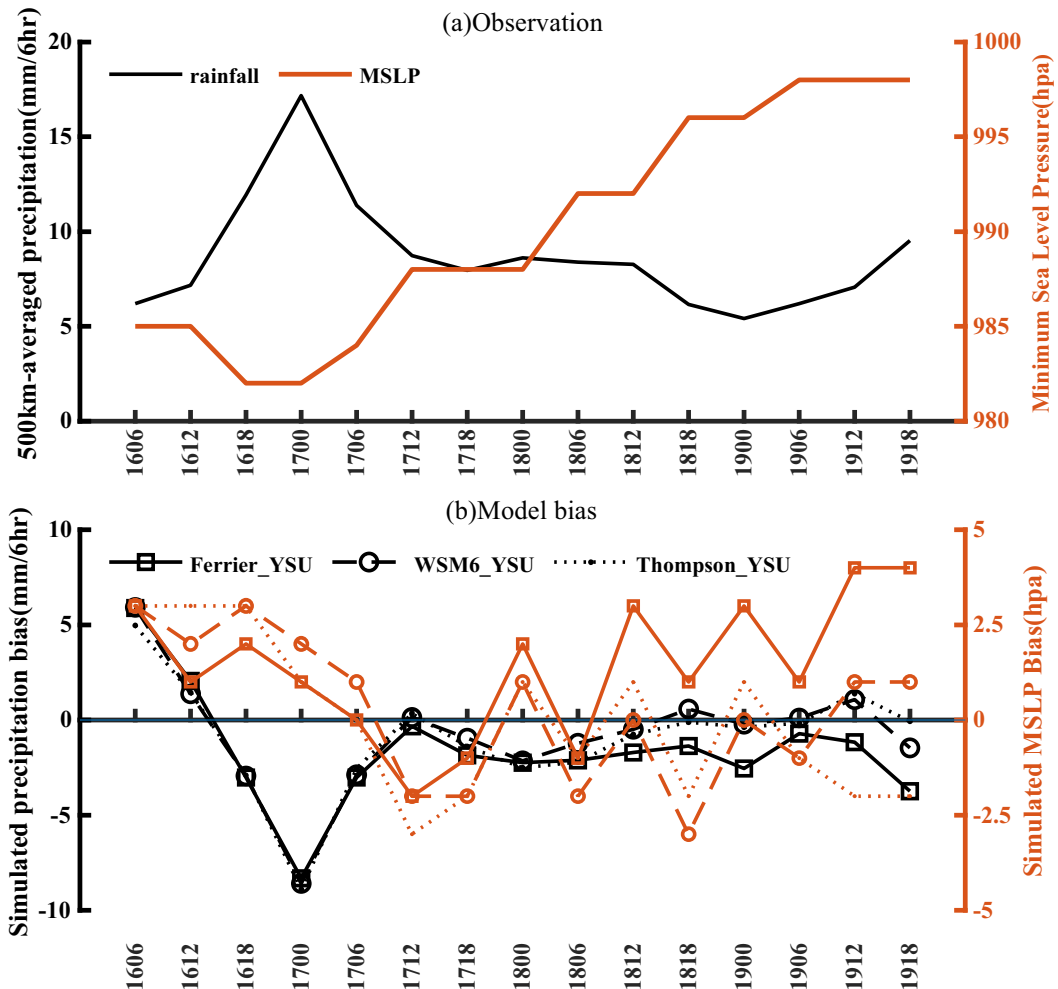


Fig. 11. (a) Time evolution of observed TC minimum sea level pressure (orange line, units: hpa) and 6-h accumulated rainfall averaged within 500 km radius from the storm center (black line, units: $\text{mm } 6^{-1}$). (b) Time evolution of simulated minimum sea level pressure bias (orange line, units: hpa) and simulated rainfall bias (black line, units: $\text{mm } 6^{-1}$) from Group_MIC_YSU with three MPs.

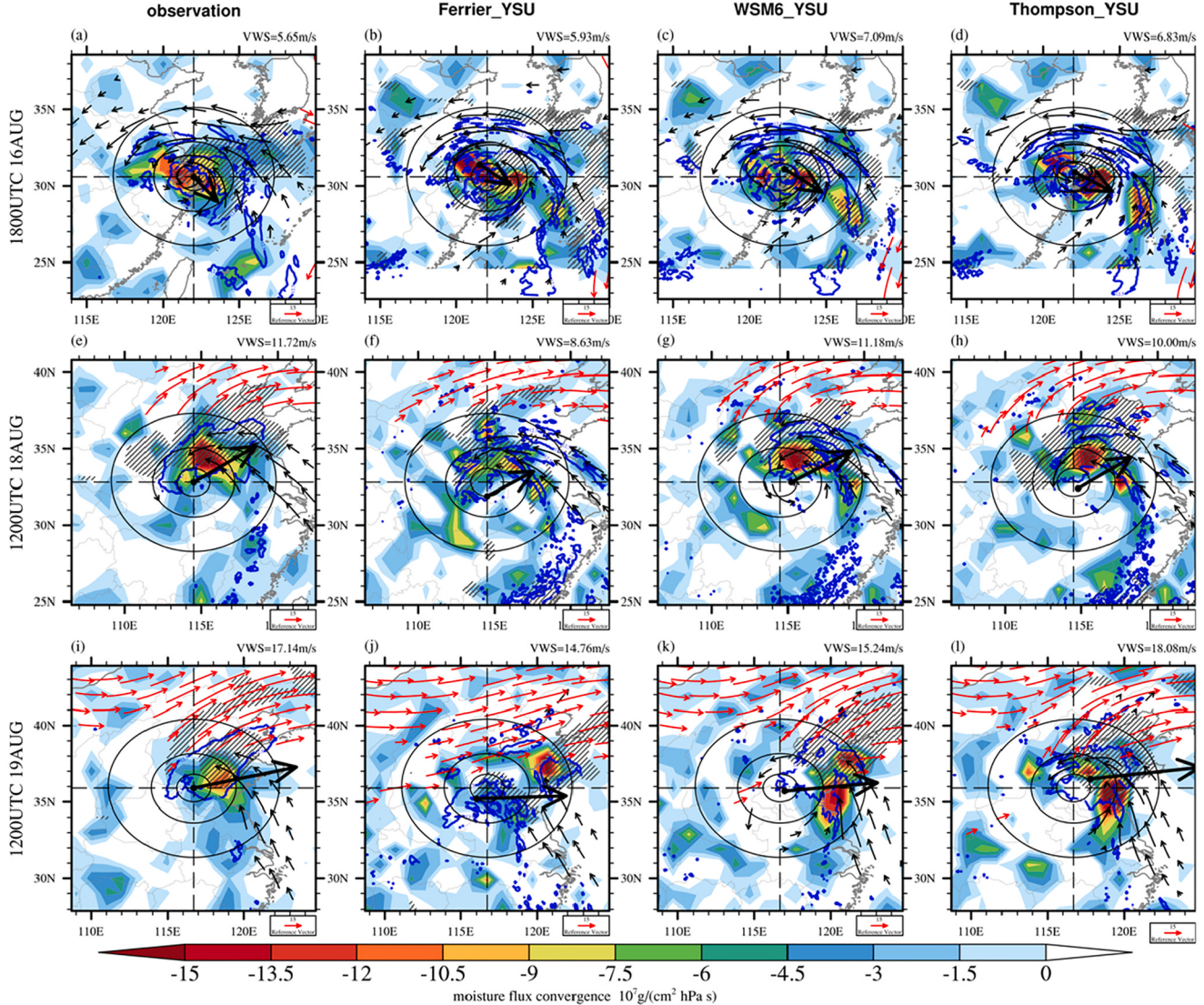


Fig. 12. The horizontal distribution of heavy rainfall (units: mm; blue solid contours, ≥ 12.5 mm for 6 h accumulation), upper-level divergence (diagonal shaded area; greater than $2.5 \cdot 10^{-5} \text{ s}^{-1}$ at 200 hPa), low-level moisture flux convergence at 925 hPa (shaded area; units: $10^7 \text{ g}/(\text{cm}^2 \cdot \text{hPa} \cdot \text{s})$) and wind field (units: m s^{-1} ; red vectors for wind $\geq 20 \text{ m s}^{-1}$ at 200 hPa, black vectors for wind $\geq 10 \text{ m s}^{-1}$ at 850 hPa) at landfall (1800 UTC 16 Aug., 2018), slow-moving stage (1200 UTC 18 Aug., 2018) and recurving stage (1200 UTC 19 Aug., 2018) from the observation and the WRF simulations using the YSU PBL scheme. The black dot denotes the TC center and the black solid arrow denotes the vertical wind shear. (For interpretation of the references to colour in this figure legend, the reader is referred to the web version of this article.)

convergence, which led to the model discrepancy in heavy rainfall forecast. At the landfall stage, the Ferrier scheme more realistically captured the magnitude of VWS and the low-level moisture convergence region, resulting in its advantages in heavy rainfall location and intensity. But it overpredicted the coverage area of upper-level wind divergence, leading to its overly scattered heavy rainfall structure.

At the two inland stages, the Ferrier MP scheme simulated the TC center position with the largest deviation and also underestimated the upper-level winds, resulting in much weaker VWS and upper-level wind divergence at the wrong position, and thus the worst performance in heavy rainfall forecast. However, the WSM6 and Thompson MP scheme mainly differed in forecasting the location and intensity of low-level moisture convergence, leading to their respective advantage at these two inland stages.

Particularly, at the slow-moving stage, the WSM6 MP scheme better captured the observed moisture convergence region and heavy rainfall area on the downshear left side within the TC inner rain band, but the Thompson scheme unrealistically produced a low-level moisture

convergence region near the outermost 500-km circle in the north of TC. At the recurving stage, the WSM6 and Thompson MP schemes both produced an unrealistic strong moisture convergence on the downshear right side contributing to their slightly overestimated intensity of heavy rainfall shown in Fig. 8. However, only the Thompson MP scheme more realistically reproduced the upper-level divergence area and better captured the low-level moisture convergence in the VWS downshear left region within the TC inner rain band, resulting in its better forecast in heavy rainfall structure and location.

5.1.3. Moisture budget and vertical velocity

We further quantified the key processes that caused the differences in the simulated radial distribution of TC heavy rainfall, including the low-level moisture budget and updrafts in TC inner and outer core regions. Fig. 13 compares the time series of simulated biases of moisture convergence at 925 hPa, upward velocity and 6-hourly accumulated rainfall averaged in the TC inner core (<100 km), the inner rain band (100–250 km) and the outer rain band (250–500 km) from

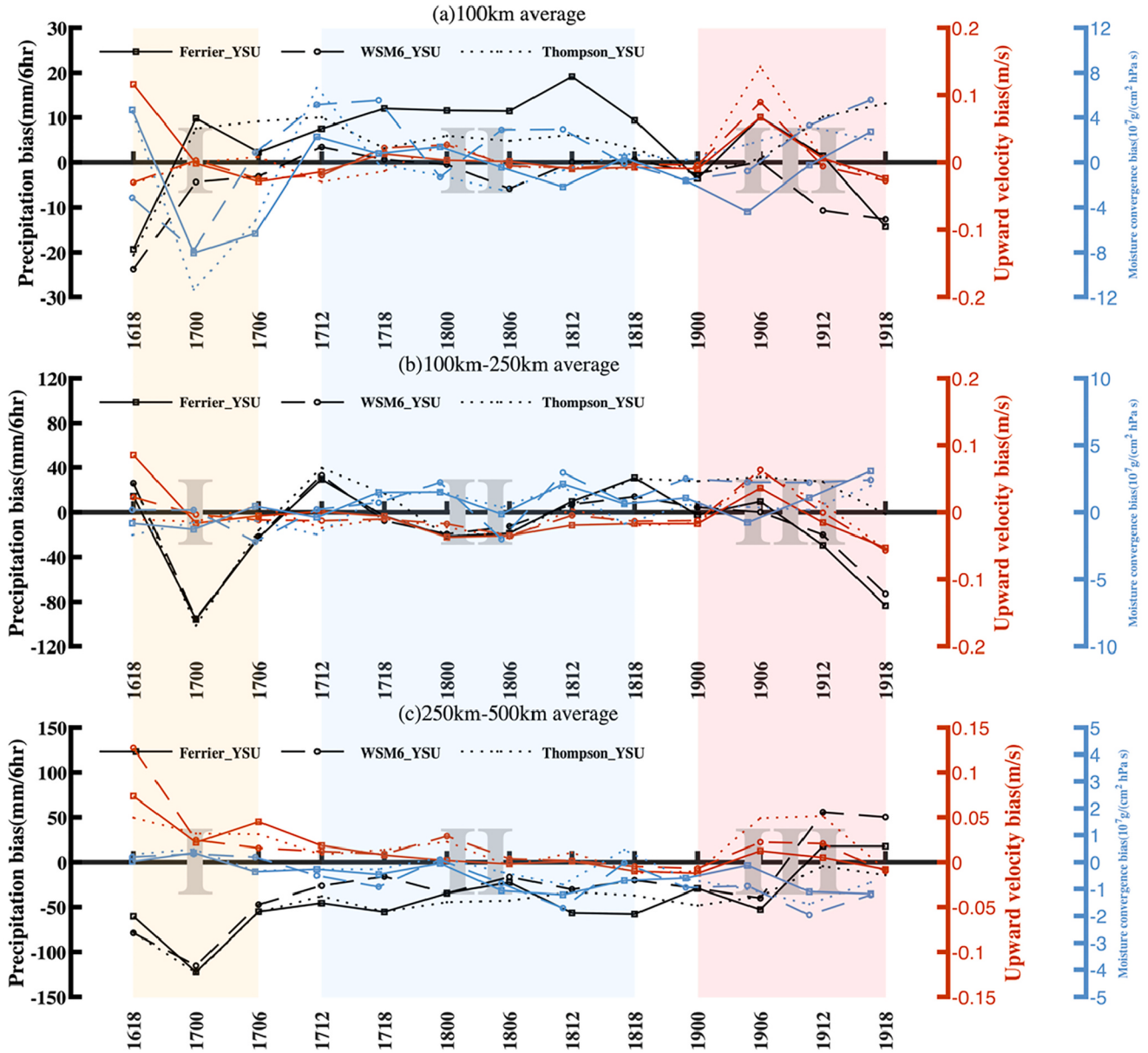


Fig. 13. Time series of simulated biases of moisture convergence (units: $10^7 \text{ g}/(\text{cm}^2 \cdot \text{hPa} \cdot \text{s})$) at 925 hPa, upward velocity (units: m s^{-1}) and accumulated rainfall (units: $\text{mm } 6 \text{ h}^{-1}$) averaged in the TC inner-core (<100 km), inner rain band (100 km–250 km) and outer rain band (250–500 km) from Group_MIC_YSU.

Group_MIC_YSU. During the landfall stage, three MP schemes all underestimated the precipitation in the inner and outer rain bands, but mainly differed in simulating the rainfall in the TC inner core, where the simulated bias of low-level moisture convergence was more consistent with the rainfall bias than the upward motion.

However, at the slow-moving stage, the simulated rainfall of three MP schemes showed no significant difference in the inner rain bands, where the rainfall bias was consistent with the simulated bias in both upward motion and low-level moisture convergence. The main differences were concentrated in the TC inner core and outer rain band. The Ferrier and Thompson scheme overestimated the rainfall in the inner core which was consistent with the bias in low-level moisture convergence, while underestimated the rainfall in the outer rain band which was consistent with the bias in upward motion. At the recurving stage, the Ferrier and WSM6 scheme underestimated the rainfall in the inner core and inner rain band, which was consistent with the bias in both upward motion and low-level moisture convergence, while the overestimated bias of rainfall in the outer rain band which was mainly

consistent with the bias in low-level moisture convergence.

Therefore, the simulated intensity of TC-induced rainfall by different MP schemes was generally regulated by the simulation of TC intensity and/or key factors related to the interaction between TC and environment, such as the strength of low-level moisture convergence and TC updrafts. Specifically, at the landfall stage with weak environmental VWS, the simulated rainfall intensity was affected more by the TC intensity and low-level moisture convergence. However, at the two inland stages with stronger environmental VWS, the simulated rainfall intensity was mainly affected by the strength of TC updrafts and/or the low-level moisture convergence in the inner core and/or the outer rain band.

5.2. Planetary boundary layer parameterization impacts

Fig. 14 shows the distance-height cross section of azimuthal mean tangential and radial winds in the northeast and southwest quadrants at three landfalling stages simulated by using the YSU and MYNN PBL

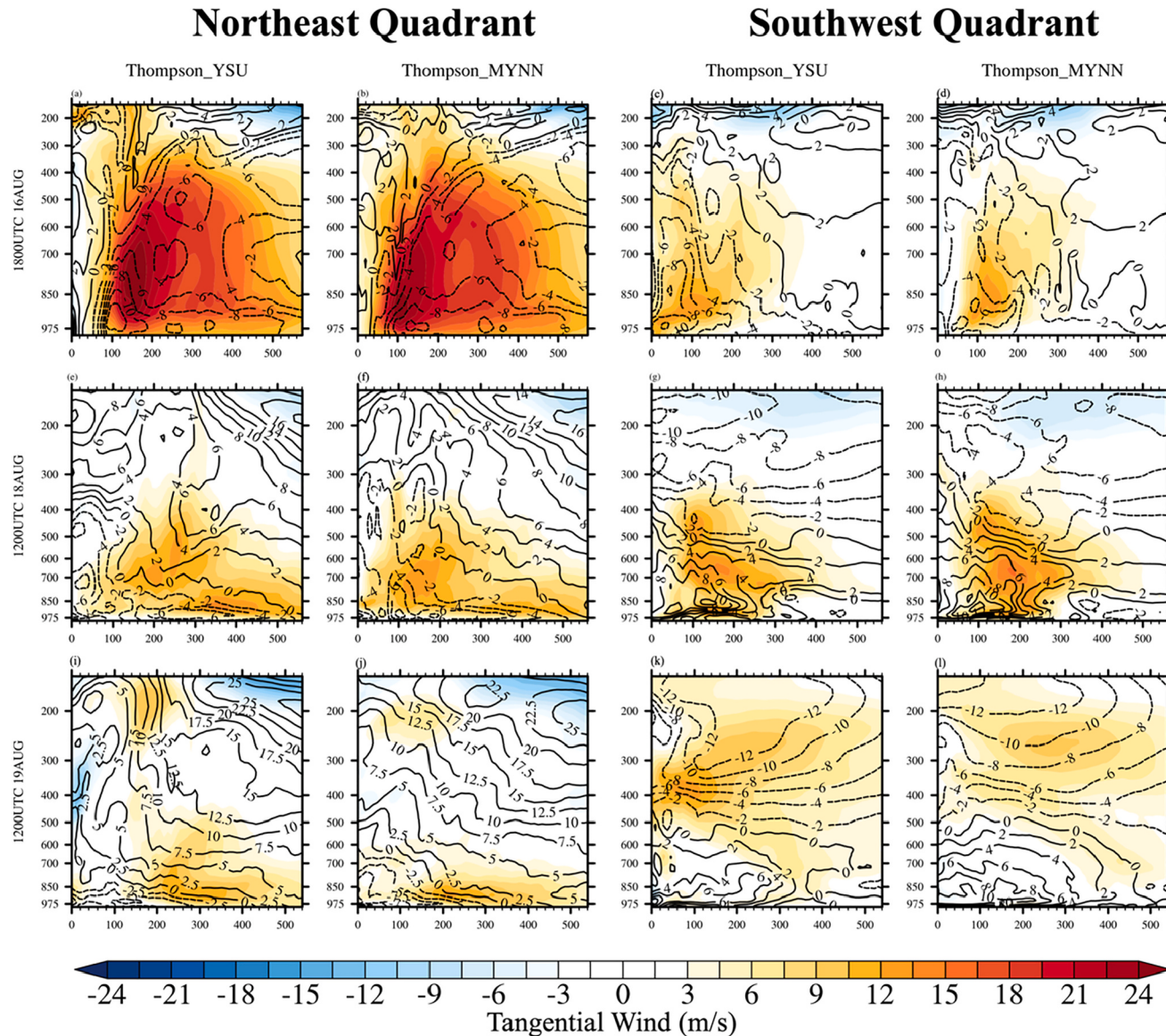


Fig. 14. Distance-height cross sections of the azimuthal mean tangential wind (shaded; units: m s^{-1}) and radial wind (contour; units: m s^{-1}) in northeast quadrant (a, b, e, f, i, j) and southwest quadrant (c, b, g, h, k, l) across the 6-h periods at three representative time between Thompson_YSU and Thompson_MYNN.

scheme. Because the PBL impacts on the TC intensity and heavy rainfall were consistent for different MPs from above analyses, hereinafter, we chose to display the simulations with the use of the Thompson MP scheme. At the landfall stage, in both simulations, the maximum tangential and radial winds were located in the northeast quadrant at about 100-km radius. Specifically, the YSU scheme systematically produced greater tangential winds and a much stronger inflow layer than the MYNN scheme, corresponding to its stronger TC intensity. As the TC Rubmia moved further inland, both the tangential and radial winds had decreased from the boundary layer to the lower troposphere. The thickness of the inflow layer decreased from 300 hPa to 850 hPa, and the outflow in the upper levels was increased. The inflow mainly occurred in the northeast quadrant, while the lower layer in the southwest quadrant was dominated by outflow.

At the slow-moving stage, the difference between the simulated wind profiles of two PBL schemes was not particularly significant, except that the YSU scheme produced a slightly stronger radial inflow wind near the eyewall in the boundary layer, which primarily contributed to its relatively stronger TC wind intensity (shown in Fig. 3); However, at the recurring stage, the impact of two PBL schemes became significant,

especially the YSU scheme produced both stronger tangential and radial winds in the upper and middle levels, which improved the TC outflow condition and thus stronger VWS that favored the TC intensification and rainfall reinforcement.

Fig. 15 compares the distance-height cross section of azimuthal mean of zonal-vertical wind and associated moisture influx and convergence as well as thermal structures from the simulations of Thompson_YSU and Thompson_MYNN as well as their differences. In both simulations, strong moisture influx and convergence region as well as larger updrafts well corresponded to the simulated heavy rainfall location within the inner core ($< 100 \text{ km}$) to the outward region ($< 250 \text{ km}$) and farther ($< 500 \text{ km}$) at different stages. Two PBL schemes mainly differed in simulating the depth of inflow moisture layer, the strength of upward motion and boundary layer TC thermal structure. Generally, the local MYNN scheme had lower vertical diffusivity in the boundary layer and thus moisture and energy were transferred upward not as efficiently as the nonlocal YSU scheme, resulting in a shallower inflow layer, weaker moisture convergence and updrafts with less latent heat released in the precipitating area.

Particularly at the two inland stages, the horizontal temperature

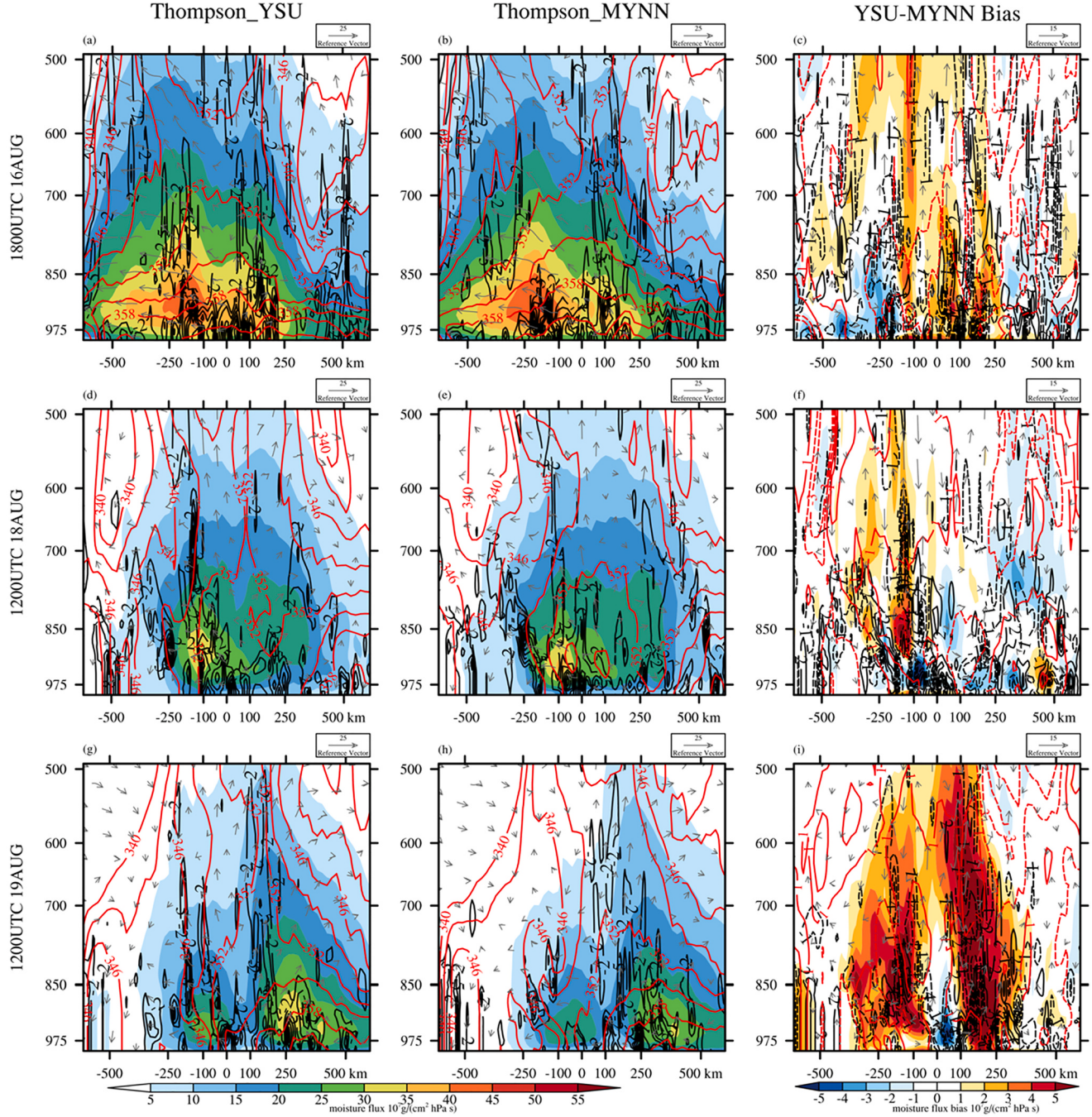


Fig. 15. (a, b, d, e, g, h) Distance-height cross sections of azimuthal mean moisture flux (shaded area; units: $\text{g}/(\text{cm} \cdot \text{hPa} \cdot \text{s})$), zonal-vertical wind field (units: m s^{-1} ; vectors; vertical velocity magnified 100 times to adapt zonal wind), equivalent potential temperature (units: K ; red solid contours) and moisture convergence (units: $10^7 \text{ g}/(\text{cm}^2 \cdot \text{hPa} \cdot \text{s})$); black contours) for the same region of the red rectangle in Figs. 5–7a averaged across the 6-h periods at three representative time between Thompson_YSU and Thompson_MYNN. (c, f, i) The bias between Thompson_YSU and Thompson_MYNN. The dashed lines denote the negative contour values. (For interpretation of the references to colour in this figure legend, the reader is referred to the web version of this article.)

gradients were smaller and thus the storm core was relatively colder in the MYNN scheme, leading to its weak baroclinic instability and thus weak convection. Especially at the recurring stage, although the MYNN scheme produced a slightly stronger moisture flux than the YSU scheme within the TC inner core near the bottom of boundary layer, it still produced much weaker low-level moisture convergence and updrafts, leading to its weaker TC and rainfall in the outer rain band.

Therefore, the local MYNN scheme had lower vertical diffusivity in the boundary layer and thus moisture and energy were transferred upward not as efficiently as the nonlocal YSU scheme, resulting in a

shallower inflow layer, weaker tangential winds and radial outflows in the upper levels, as well as weaker low-level moisture convergence and updrafts. This led to that the MYNN scheme systematically produced weaker TC and precipitation for all three stages than the YSU scheme. This was also supported by previous studies such as Dong et al. (2019). Meanwhile, compared to the YSU scheme, the MYNN scheme particularly produced weaker environmental VWS, which was a key factor regulating the heavy rainfall location and structure in the two inland stages as shown in Figs. 6 and 7. As such, the MYNN scheme further increased the underestimated TC intensity errors by the YSU scheme at

landfall, and largely degraded the simulations of heavy rainfall location and structure at the two inland stages.

6. Conclusions and discussions

In this study, the weak sustained tropical cyclone (TC) Rumbia (2018) and its induced widespread heavy rainfall after landfall was simulated using the WRF model at 3-km grid. Two groups of WRF experiments were conducted based on the use of three MPs (Ferrier, WSM6 and Thompson) and two different PBL schemes (YSU and MYNN) respectively. We examined the impacts of multi-physics parameterizations on the simulations of TC track, intensity and heavy rainfall distributions at landfall, inland slow-moving and recurring stages. The Structure-Amplitude-Location (SAL) technique was specifically used to quantitatively evaluate the forecast skills of heavy rainfall ($\geq 12.5 \text{ mm}/6 \text{ h}$) at different stages. The focus was on investigating the key factors and physical processes regulating the distribution of heavy rainfall of landed TC Rumbia and their sensitivities to different microphysics and planetary boundary layer schemes. The main conclusions were summarized with discussions as below.

First, the distribution of heavy rainfall at landfall was largely regulated by the intensity of TC itself, but then more affected by environmental factors at the two inland stages, mainly including the environmental VWS, TC updrafts and associated upper-level wind divergence and low-level moisture convergence. Specifically, at landfall stage (with relatively weak VWS), heavy rainfall was located in the TC inner core and inner rain band on the upshear side, and its intensity was affected more by the TC intensity and low-level moisture convergence. However, at the inland stages (with stronger VWS), heavy rainfall was located in the TC outer core region on the downshear left side, well corresponding to the coverage of upper-level wind divergence and low-level moisture convergence, and its intensity was affected by the strength of both low-level moisture convergence and TC updrafts in the outer core region.

Second, three microphysical schemes mainly differed in the simulation of ice-phased particles and the radial distribution of diabatic heating at three different landing stages, which affected the simulation of TC thermodynamic structure and key environmental factors, leading to the different simulations of TC intensity and heavy rainfall distribution. Specifically, at the landfall stage, the Ferrier scheme showed a slight advantage in simulating the intensity of both TC and heavy rainfall, because it produced the largest amount of upper-level cloud ice with strong diabatic heating rate in the TC inner core, and better captured the weak VWS and the inner-core low-level moisture convergence on the upshear side. But this advantage disappeared soon after landing and the Ferrier scheme severely underestimated the TC intensity and the key environmental factors (VWS and upper-level divergence), showing the worst performance in heavy rainfall forecast. However, at the two inland stages, the WSM6 and Thompson schemes simulated the TC intensity better than the Ferrier scheme because they produced more graupel or snow with stronger diabatic heating rate from the inner core to the inner rainband. Particularly, they better simulated the stronger VWS and downshear-left upper-level wind divergence and low-level moisture convergence, leading to their respective advantages in capturing the structure and location of postlandfall heavy rainfall.

Third, the YSU and MYNN schemes mainly differed in simulating the strength and depth of inflow layer, the vertical distribution of tangential and radial winds, and the strength of low-level moisture flux and upward motions, which affected the simulation of the intensity of TC and heavy rainfall after landfall. Specifically, the local MYNN scheme had lower vertical diffusivity in the boundary layer and thus moisture and energy were transferred upward not as efficiently as the nonlocal YSU scheme, resulting in a shallower inflow layer, weaker tangential winds and radial outflows in the upper levels, as well as weaker low-level moisture convergence and upward motions. This led to the MYNN scheme not only underestimating TC intensity and heavy rainfall at all three stages

more than the YSU scheme, but also generating weaker environmental VWS which largely degraded the simulation of heavy rainfall location and structure at the two inland stages.

The purpose of this study goes beyond the individual case, but to complement and expand the previous sensitivity studies for weak landfalling TCs which brought extreme precipitation. We intended to improve our understanding of different WRF model physical parameterization schemes and their interplay impacts on the high-resolution simulations of heavy rainfall induced by weak landfalling TC Rumbia. But limitations in our study are needed to be pointed out. For example, we tested the three-level nesting approach from 27 km to 3 km, but found that 3-km single nesting showed advantages in simulating the landed TC rainfall in this case. Therefore, we used the downscaling method similar to the study of Nasrollahi et al. (2012) in which 1° GFS data were used as initial and lateral boundary conditions to drive the WRF model at 4-km grid to simulate the Hurricane Rita (2005). The effect of low-resolution initial conditions on the model results is usually short and not significant, especially for the strong synoptic-scale conditions, such as the landfall TC (Vie et al., 2011). But the model errors in our simulations should be noted that they included the errors from nonlinear effects of domain setup and the steep lateral downscaling from 1° NCEP FNL on the 3-km WRF grids.

In addition to the sensitivity to these different physical processes, accurate landed TC precipitation forecast also depends on other physical setting, grid resolution and observations. The presented results should be considered as relative comparisons to the best approximation of the observations available. For instance, the surface layer parameterization is also critical for the TC simulation regarding the surface and boundary layer exchange, and thus different surface parameterization and their interaction with PBL schemes should be considered. If more observations of in-cloud hydrometeors can be achieved, current microphysics schemes such as Ferrier, WSM6 or Thompson with specific advantages in different landing stages, can be further adjusted according to the deviations identified.

Declaration of Competing Interest

The authors declare that they have no known competing financial interests or personal relationships that could have appeared to influence the work reported in this paper.

Acknowledgements

This research was supported by the National Natural Science Foundation for Young Scientist of China (Grant No. 41605079), Shanghai 2021 “Scientific and technological innovation action plan” Natural Science Foundation (Grant No. 21ZR1420400), and National Key R&D Program of China (Grant No. 2018YFC1507702). The Final (FNL) Operational Global Analysis data at 1° grids provided by National Centers for Environmental Prediction (NCEP) is used in this study and can be found in <https://rda.ucar.edu/datasets/ds083.2/index.html>. The best track data from Shanghai Typhoon Institute of China Meteorological Administration (STI/CMA) could be found in http://tcdatalyphoon.org.cn/zjljsjj_sm.html. And the Half Hourly $0.1^\circ \times 0.1^\circ$ rainfall products from the Integrated Multi-satellite Retrievals for GPM-Global Precipitation Measurement Mission (IMERG) could be found in https://disc.gsfc.nasa.gov/datasets/GPM_3IMERGHH_06/summary. The model simulations were conducted at the ECNU Multifunctional Platform for Innovation 001 facilities and data was deposited in ECNU public data server with IP 49.52.29.112. The views expressed are those of the authors and do not necessarily reflect those of the sponsoring agencies.

References

- Atallah, E., Bosart, L.F., Aiyer, A.R., 2007. Precipitation distribution associated with landfalling tropical cyclones over the eastern United States. *Mon. Weather Rev.* 135 (6), 2185–2206. <https://doi.org/10.1175/mwr3382.1>.
- Bao, X., Wu, L., Tang, B., Ma, L., Wu, D., Tang, J., et al., 2019. Variable raindrop size distributions in different rainbands associated with Typhoon Fitow (2013). *J. Geophys. Res.-Atmos.* 124 (22), 12262–12281. <https://doi.org/10.1029/2019jd030268>.
- Barnston, A.G., 1992. Correspondence among the correlation, RMSE, and Heidke forecast verification measures; refinement of the Heidke score. *Weather Forecast.* 7 (4), 699–709. <http://dx.doi.org/>. [https://doi.org/10.1175/1520-0434\(1992\)0072.0.CO;2](https://doi.org/10.1175/1520-0434(1992)0072.0.CO;2).
- Bender, M.A., 1997. The effect of relative flow on the asymmetric structure in the interior of hurricanes. *J. Atmos. Sci.* 54, 703–724. [https://doi.org/10.1175/1520-0469\(1997\)054<0703:TEORFO>2.0.CO;2](https://doi.org/10.1175/1520-0469(1997)054<0703:TEORFO>2.0.CO;2).
- Braun, S.A., Tao, W.K., 2000. Sensitivity of high-resolution simulations of Hurricane Bob (1991) to planetary boundary layer parameterizations. *Mon. Weather Rev.* 128 (12), 3941–3961. [https://doi.org/10.1175/1520-0493\(2000\)129<3941:Sohrso>2.0.Co;2](https://doi.org/10.1175/1520-0493(2000)129<3941:Sohrso>2.0.Co;2).
- Cecil, D.J., 2007. Satellite-derived rain rates in vertically sheared tropical cyclones. *Geophys. Res. Lett.* 34 (2) <https://doi.org/10.1029/2006gl027942>.
- Chen, L., Ding, Y., 1979. An Introduction to Typhoons in the Western Pacific (in Chinese). Science Press, Beijing, China, pp. 179–181.
- Chen, S.Y.S., Knaff, J.A., Marks, F.D., 2006. Effects of vertical wind shear and storm motion on tropical cyclone rainfall asymmetries deduced from TRMM. *Mon. Weather Rev.* 134 (11), 3190–3208. <https://doi.org/10.1175/mwr3245.1>.
- Chen, L.S., Li, Y., Cheng, Z.Q., 2010. An overview of research and forecasting on rainfall associated with landfalling tropical cyclones. *Adv. Atmos. Sci.* 27 (5), 967–976. <https://doi.org/10.1007/s00376-010-8171-y>.
- Chen, S.M., Qian, Y.K., Peng, S.Q., 2015. Effects of various combinations of boundary layer schemes and microphysics schemes on the track forecasts of tropical cyclones over the South China Sea. *Nat. Hazards* 78 (1), 61–74. <https://doi.org/10.1007/s11069-015-1697-7>.
- Chen, G., Wu, C.C., Huang, Y.H., 2018. The role of near-core convective and stratiform heating/cooling in tropical cyclone structure and intensity. *J. Atmos. Sci.* 75 <https://doi.org/10.1175/JAS-D-1117-0122.1171>.
- Colle, B.A., 2003. Numerical Simulations of the extratropical transition of Floyd (1999): structural evolution and responsible mechanisms for the heavy rainfall over the northeast United States. *Mon. Weather Rev.* 131 (12), 2905–2926. [https://doi.org/10.1175/1520-0493\(2003\)131<2905:Nsotet>2.0.Co;2](https://doi.org/10.1175/1520-0493(2003)131<2905:Nsotet>2.0.Co;2).
- Cox, G., 1988. Modelling precipitation in frontal rainbands. *Q. J. R. Meteorol. Soc.* 114, 115–127.
- Davis, C., Bosart, L.F., 2002. Numerical simulations of the genesis of Hurricane Diana (1984). Part II: sensitivity of track and intensity prediction. *Mon. Weather Rev.* 130 (5), 1100–1124. [https://doi.org/10.1175/1520-0493\(2002\)130<1100:Nsotgo>2.0.Co;2](https://doi.org/10.1175/1520-0493(2002)130<1100:Nsotgo>2.0.Co;2).
- Dong, M.Y., Ji, C.X., Chen, F., Wang, Y.Q., 2019. Numerical study of boundary layer structure and rainfall after landfall of Typhoon Fitow (2013): sensitivity to planetary boundary layer parameterization. *Adv. Atmos. Sci.* 36 (4), 431–450. <https://doi.org/10.1007/s00376-018-7281-9>.
- Dudhia, J., 1989. Numerical study of convection observed during the Winter Monsoon Experiment using a mesoscale two-dimensional model. *J. Atmos. Sci.* 46, 3077–3107.
- Feng, X.B., Shu, S.J., 2018. How do weak tropical cyclones produce heavy rainfall when making landfall over China. *J. Geophys. Res.-Atmos.* 123 (21), 11830–11848. <https://doi.org/10.1029/2018jd029228>.
- Field, P.R., Hogan, R.J., Brown, P.R.A., Illingworth, A.J., Choularton, T.W., Cotton, R.J., 2005. Parameterization of ice-particle size distributions for mid-latitude stratiform cloud. *Q. J. R. Meteorol. Soc.* 131 (609), 1997–2017. <https://doi.org/10.1256/qj.04.134>.
- Fovell, R.G., Su, H., 2007. Impact of cloud microphysics on hurricane track forecasts. *Geophys. Res. Lett.* 34.
- Fovell, R.G., Bu, Y.P., Corbosiero, K.L., Tung, W.W., Cao, Y., Kuo, H.C., et al., 2016. Influence of cloud microphysics and radiation on tropical cyclone structure and motion. *Meteorol. Monogr.* 56, 11.11–11.27.
- Gao, S.Z., Meng, Z.Y., Zhang, F.Q., Bosart, L.F., 2009. Observational analysis of heavy rainfall mechanisms associated with severe tropical storm bilis (2006) after Its Landfall. *Mon. Weather Rev.* 137 (6), 1881–1897. <https://doi.org/10.1175/2008mwr2669.1>.
- Ge, X.Y., Li, T., Zhang, S.J., Peng, M., 2010. What causes the extremely heavy rainfall in Taiwan during Typhoon Morakot (2009)? *Atmos. Sci. Lett.* 11 (1), 46–50. <https://doi.org/10.1002/asl.255>.
- Han, J.Y., Hong, S.Y., 2018. Precipitation forecast experiments using the Weather Research and Forecasting (WRF) model at gray-zone resolutions. *Weather Forecast.* 33 (6), 1605–1616. <https://doi.org/10.1175/waf-d-18-0026.1>.
- Hence, D.A., Houze, R.A., 2012. Vertical structure of tropical cyclone rainbands as seen by the TRMM precipitation radar. *J. Atmos. Sci.* 69 (9), 2644–2661. <https://doi.org/10.1175/jas-d-11-0323.1>.
- Hong, S.Y., Lim, J.O.J., 2006. The WRF single-moment 6-class microphysics scheme (WSM6). *J. Korean Meteor. Soc.* 42, 129–151.
- Hong, S.Y., Noh, Y., Dudhia, J., 2006. A new vertical diffusion package with an explicit treatment of entrainment processes. *Mon. Weather Rev.* 134 (9), 2318–2341. <https://doi.org/10.1175/mwr3199.1>.
- Huffman, G.J., Stocker, E.F., Bolvin, D.T., Nelkin, E.J., Tan, Jackson, 2019. GPM IMERG Final Precipitation L3 Half Hourly 0.1 Degree x 0.1 Degree V06. Goddard Earth Sciences Data and Information Services Center (GES DISC), Greenbelt, MD. <https://doi.org/10.5067/GPM/IMERG/3B-HH/06>.
- Janjić, Z.I., 1994. The step-mountain eta coordinate model: further developments of the convection, viscous sublayer, and turbulence closure schemes. *Mon. Weather Rev.* 122 (5), 927–945. [https://doi.org/10.1175/1520-0493\(1994\)122%3c0927:TSMECM%3e2.0.CO;2](https://doi.org/10.1175/1520-0493(1994)122%3c0927:TSMECM%3e2.0.CO;2).
- Jimenez, Pedro A., Dudhia, Jimy, Gonzalez-Rouco, J. Fidel, Navarro, Jorge, Montávez, Juan P., García-Bustamante, Elena, 2012. A revised scheme for the WRF surface layer formulation. *Mon. Weather Rev.* 140, 898–918 d forecasting/16th conference on numerical weather prediction, pp. 11–15.
- Jin, Y., Wang, S.P., Nachamkin, J., Doyle, J.D., Thompson, G., Grasso, L., et al., 2014. The impact of ice phase cloud parameterizations on tropical cyclone prediction. *Mon. Weather Rev.* 142 (2), 606–625. <https://doi.org/10.1175/mwr-d-13-0058.1>.
- Jones, S.C., Harr, P.A., Abraham, J., Bosart, L.F., Bowyer, P.J., Evans, J.L., et al., 2003. The extratropical transition of tropical cyclones: Forecast challenges, current understanding, and future directions. *Weather Forecast.* 18 (6), 1052–1092. [https://doi.org/10.1175/1520-0434\(2003\)018<1052:Tetoc>2.0.Co;2](https://doi.org/10.1175/1520-0434(2003)018<1052:Tetoc>2.0.Co;2).
- Kepert, J.D., 2012. Choosing a boundary layer parameterization for tropical cyclone modeling. *Mon. Weather Rev.* 140 (5), 1427–1445. <https://doi.org/10.1175/mwr-d-11-00217.1>.
- Komaromi, W.A., Doyle, J.D., 2018. On the dynamics of tropical cyclone and trough interactions. *J. Atmos. Sci.* 75 (8), 2687–2709. <https://doi.org/10.1175/jas-d-17-0272.1>.
- Li, X.L., Pu, Z.X., 2008. Sensitivity of numerical simulation of early rapid intensification of Hurricane Emily (2005) to cloud microphysical and planetary boundary layer parameterizations. *Mon. Weather Rev.* 136 (12), 4819–4838. <https://doi.org/10.1175/2008mwr2366.1>.
- Li, X.L., Pu, Z.X., 2009. Sensitivity of numerical simulations of the early rapid intensification of hurricane emily to cumulus parameterization schemes in different model horizontal resolutions. *J. Meteorol. Soc. Jpn.* 87 (3), 403–421. <https://doi.org/10.2151/jmsj.87.403>.
- Li, Q., Wang, Y., Duan, Y., 2014. Effects of diabatic heating and cooling in the rapid filamentation zone on structure and intensity of a simulated tropical cyclone. *J. Atmos. Sci.* 71, 3144–3163. <https://doi.org/10.1175/JAS-D-13-0312.1>.
- Li, Y.B., Cheung, K.K.W., Chan, J.C.L., 2015. Modelling the effects of land-sea contrast on tropical cyclone precipitation under environmental vertical wind shear. *Q. J. R. Meteorol. Soc.* 141 (687), 396–412. <https://doi.org/10.1002/qj.2359>.
- Ling, Z., Wang, Y.Q., Wang, G.H., 2016. Impact of intraseasonal oscillations on the activity of tropical cyclones in summer over the South China Sea. Part I: local tropical cyclones. *J. Clim.* 29 (2), 855–868. <https://doi.org/10.1175/jcli-d-15-0617.1>.
- Liu, J.J., Zhang, F.M., Pu, Z.X., 2017. Numerical simulation of the rapid intensification of Hurricane Katrina (2005): sensitivity to boundary layer parameterization schemes. *Adv. Atmos. Sci.* 34 (4), 482–496. <https://doi.org/10.1007/s00376-016-6209-5>.
- Locatelli, J.D., Hobbs, P.V., 1974. Fall speeds and masses of solid precipitation particles. *J. Geophys. Res.* 79, 2185–2197.
- Lonfat, M., Marks, F.D., Chen, S.Y.S., 2004. Precipitation distribution in tropical cyclones using the Tropical Rainfall Measuring Mission (TRMM) Microwave Imager: a global perspective. *Mon. Weather Rev.* 132 (7), 1645–1660. [https://doi.org/10.1175/1520-0493\(2004\)132<1645:Pditcu>2.0.Co;2](https://doi.org/10.1175/1520-0493(2004)132<1645:Pditcu>2.0.Co;2).
- Lord, S.J., Lord, J.M., 1988. Vertical velocity structures in an axisymmetric, nonhydrostatic tropical cyclone model. *J. Atmos. Sci.* 45 (9), 1453–1461.
- May, T.P., Kepert, J.D., Keenan, T.D., 2008. Polarimetric radar observations of the persistently asymmetric structure of Tropical Cyclone Ingrid. *Mon. Weather Rev.* 136 (2), 616–630. <https://doi.org/10.1175/2007mwr2077.1>.
- McFarquhar, G.M., Zhang, H.N., Heymsfield, G., Hood, R., Dudhia, J., Halverson, J.B., et al., 2006. Factors affecting the evolution of Hurricane Erin (2001) and the distributions of hydrometeors: role of microphysical processes. *J. Atmos. Sci.* 63 (1), 127–150. <https://doi.org/10.1175/jas3590.1>.
- Mellor, G.L., Yamada, T., 1982. Development of a turbulence closure model for geophysical fluid problems. *Rev. Geophys.* 20 (4), 851–875.
- Meng, W.G., Wang, Y.Q., 2016a. A diagnostic study on heavy rainfall induced by landfalling Typhoon Utor (2013) in South China: 2. postlandfall rainfall. *J. Geophys. Res.-Atmos.* 121 (21), 12803–12819. <https://doi.org/10.1002/2015jd024647>.
- Meng, W.G., Wang, Y.Q., 2016b. A diagnostic study on heavy rainfall induced by Typhoon Utor (2013) in South China: 1. Rainfall asymmetry at landfall. *J. Geophys. Res.-Atmos.* 121 (21), 12781–12802. <https://doi.org/10.1002/2015jd024646>.
- Flower, Eli J., Taubman, Steven J., Brown, Patrick D., Iacono, M.J., Clough, S.A., 1997. Radiative transfer for inhomogeneous atmospheres: RRTM, a validated correlated-k model for the longwave. *J. Geophys. Res.* 102, 16663–16682.
- Nakanishi, M., Niino, H., 2006. An improved mellor-yamada level-3 model: Its numerical stability and application to a regional prediction of advection fog. *Bound.-Layer Meteorol.* 119 (2), 397–407. <https://doi.org/10.1007/s10546-005-9030-8>.
- Nakanishi, M., Niino, H., 2009. Development of an improved turbulence closure model for the atmospheric boundary layer. *J. Meteorol. Soc. Jpn.* 87 (5), 895–912. <https://doi.org/10.2151/jmsj.87.895>.
- Nasrollahi, N., AghaKouchak, A., Li, J.L., Gao, X.G., Hsu, K.L., Sorooshian, S., 2012. Assessing the impacts of different WRF precipitation physics in hurricane simulations. *Weather Forecast.* 27 (4), 1003–1016. <https://doi.org/10.1175/waf-d-10-05000.1>.
- NOAA, 2010. National Oceanic and Atmospheric Administration Changes to the NCEP Meso Eta Analysis and Forecast System: Increase in Resolution, New Cloud Microphysics, Modified Precipitation Assimilation, Modified 3DVAR Analysis. Available online at: <http://www.emc.ncep.noaa.gov/mmb/mmbpl1/eta12tpb/>.
- Nolan, D.S., Zhang, J.A., Stern, D.P., 2009a. Evaluation of planetary boundary layer parameterizations in tropical cyclones by comparison of in situ observations and

- high-resolution simulations of Hurricane Isabel (2003). Part I: initialization, maximum winds, and the Outer-Core Boundary Layer. *Mon. Weather Rev.* 137, 3651–3674. <https://doi.org/10.1175/2009mwr2785.1>.
- Nolan, D.S., Zhang, J.A., Stern, D.P., 2009b. Evaluation of planetary boundary layer parameterizations in tropical cyclones by comparison of in situ observations and high-resolution simulations of Hurricane Isabel (2003). Part II: inner-core boundary layer and eyewall structure. *Mon. Weather Rev.* 137, 3675–3698. <https://doi.org/10.1175/2009mwr2786.1>.
- Pang, Q., Ping, F., Shen, X., Liu, L., 2019. A comparative study of effects of different microphysics schemes on precipitation simulation for Typhoon Mujigae(2015). *Chin. J. Atmos. Sci.* 43 (1), 202–220. <https://doi.org/10.3878/j.issn.1006-9895.1804.17291>.
- Rajeswari, J.R., Srinivas, C.V., Mohan, P.R., Venkatraman, B., 2020. Impact of boundary layer physics on tropical cyclone simulations in the Bay of Bengal using the WRF model. *Pure Appl. Geophys.* 177 (11), 5523–5550.
- Rajapakse, P.V.S., Pottu, J., Mohanty, U.C., 2011. Sensitivity of physical parameterizations on prediction of tropical cyclone Nargis over the Bay of Bengal using WRF model. *Meteorog. Atmos. Phys.* 113 (3–4), 125–137. <https://doi.org/10.1007/s00703-011-0151-y>.
- Shapiro, L.J., 1983. The asymmetric boundary layer flow under a translating hurricane. *J. Atmos. Sci.* 40 (8) [https://doi.org/10.1175/1520-0469\(1983\)040<1984:TABLFU>2.0.CO;2](https://doi.org/10.1175/1520-0469(1983)040<1984:TABLFU>2.0.CO;2).
- Shu, S.J., Zhang, F.Q., Ming, J., Wang, Y., 2014. Environmental influences on the intensity changes of tropical cyclones over the western North Pacific. *Atmos. Chem. Phys.* 14 (12), 6329–6342. <https://doi.org/10.5194/acp-14-6329-2014>.
- Skamarock, W.C., Klemp, J.B., Dudhia, J., Gill, D.O., Barker, D.M., Duda, M.G., Huang, X.-Y., Wang, W., Powers, J.G., 2008. A Description of the Advanced Research WRF Version 3. NCAR Tech. Note NCAR/TN-475+STR, (113 pp).
- Smith, R.K., Thomsen, G.L., 2010. Dependence of tropical cyclone intensification on the boundary-layer representation in a numerical model. *Q. J. R. Meteorol. Soc.* 136 (652), 1671–1685. <https://doi.org/10.1002/qj.687>.
- Starr, D.O.C., Cox, S.K., 1985. Cirrus clouds. Part I: a cirrus cloud model. *J. Atmos. Sci.* 42, 2663–2681. [https://doi.org/10.1175/1520-0469\(1985\)042<2663:Ccipac>2.0.Co;2](https://doi.org/10.1175/1520-0469(1985)042<2663:Ccipac>2.0.Co;2).
- Stensrud, D.J., 2009. Parameterization Schemes: Keys to Understanding Numerical Weather Prediction Models. Cambridge University Press.
- Sun, Y., Zhong, Z., Lu, W., 2015. Sensitivity of tropical cyclone feedback on the intensity of the western Pacific subtropical high to microphysics schemes. *J. Atmos. Sci.* 72, 1346–1368.
- Tao, W.K., Shi, J.J., Chen, S.S., Lang, S., Lin, P.L., Hong, S.Y., et al., 2011. The impact of microphysical schemes on hurricane intensity and track. *Asia-Pac. J. Atmos. Sci.* 47, 1–16.
- Tewari, M., Chen, F., Wang, W., Dudhia, J., LeMone, M.A., Mitchell, K., Ek, M., Gayno, G., Wegiel, J., Cuenca, R.H., 2004. Implementation and verification of the unified NOAH land surface model in the WRF model. In: 20th Conference on Weather Analysis, pp. 11–15.
- Thompson, G., Field, P.R., Rasmussen, R.M., Hall, W.D., 2008. Explicit forecasts of winter precipitation using an improved bulk microphysics scheme. Part II: implementation of a new snow parameterization. *Mon. Weather Rev.* 136 (12), 5095–5115. <https://doi.org/10.1175/2008mwr2387.1>.
- Vie, B., Nuissier, O., Ducrocq, V., 2011. Cloud-resolving ensemble simulations of Mediterranean heavy precipitating events: uncertainty on initial conditions and lateral boundary conditions. *Mon. Weather Rev.* 139 (2), 403–423.
- Wang, Y.Q., 2002. An explicit simulation of tropical cyclones with a triply nested movable mesh primitive equation model: TCM3. Part II: model refinements and sensitivity to cloud microphysics parameterization. *Mon. Weather Rev.* 130 (12), 3022–3036. [https://doi.org/10.1175/1520-0493\(2002\)130<3022:Aesotc>2.0.Co;2](https://doi.org/10.1175/1520-0493(2002)130<3022:Aesotc>2.0.Co;2).
- Wang, Y.Q., 2009. How do outer spiral rainbands affect tropical cyclone structure and intensity? *J. Atmos. Sci.* 66, 1250–1273. <https://doi.org/10.1175/2008JAS2737.1>.
- Wang, C., 2013. Experiments of influence of planetary boundary layer parameterization on Muifa Typhoon prediction. *Adv. Earth Science* 28 (2), 197–208. <https://doi.org/10.11867/j.issn.1001-8166.2013.02.0197>.
- Wang, Y.Q., Holland, G.J., 1996. Tropical cyclone motion and evolution in vertical shear. *J. Atmos. Sci.* 53 (22), 3313–3332. [https://doi.org/10.1175/1520-0469\(1996\)053<3313:Tcmrei>2.0.Co;2](https://doi.org/10.1175/1520-0469(1996)053<3313:Tcmrei>2.0.Co;2).
- Wang, R., Zhu, Y.T., Qiao, F.X., Liang, X.Z., Zhang, H., Ding, Y., 2021. High-resolution simulation of an extreme heavy rainfall event in shanghai using the weather research and forecasting model: sensitivity to planetary boundary layer parameterization. *Adv. Atmos. Sci.* 38 (1), 98–115.
- Weisman, M.L., Skamarock, W.C., Klemp, J.B., 1997. The resolution dependence of explicitly modeled convective systems. *Mon. Weather Rev.* 125 (4), 527–548. [https://doi.org/10.1175/1520-0493\(1997\)125<0527:Trdoem>2.0.Co;2](https://doi.org/10.1175/1520-0493(1997)125<0527:Trdoem>2.0.Co;2).
- Wernli, H., Paulat, M., Hagen, M., Frei, C., 2008. SAL-A novel quality measure for the verification of quantitative precipitation forecasts. *Mon. Weather Rev.* 136 (11), 4470–4487. <https://doi.org/10.1175/2008mwr2415.1>.
- Wilks, D.S., 2011. Statistical Methods in the Atmospheric Sciences. <https://doi.org/10.1080/00401706.1996.10484553>.
- Willetts, P.D., Marsham, J.H., Birch, C.E., Parker, D.J., Webster, S., Petch, J., 2017. Moist convection and its upscale effects in simulations of the Indian monsoon with explicit and parametrized convection. *Q. J. R. Meteorol. Soc.* 143 (703), 1073–1085. <https://doi.org/10.1002/qj.2991>.
- Willoughby, H.E., Jin, H.-L., Lord, S.J., Piotrowicz, J.M., 1984. Hurricane structure and evolution as simulated by an axisymmetric, nonhydrostatic numerical model. *J. Atmos. Sci.* 41 (7), 1169–1186.
- Wu, L.G., Liang, J., Wu, C.C., 2011. Monsoonal influence on Typhoon Morakot (2009). Part I: observational analysis. *J. Atmos. Sci.* 68 (10), 2208–2221. <https://doi.org/10.1175/2011jas3730.1>.
- Wu, D., Zhao, K., Kumjian, M.R., Chen, X., Huang, H., Wang, M., et al., 2018. Kinematics and microphysics of convection in the outer rainband of typhoon nida (2016) revealed by polarimetric radar. *Mon. Weather Rev.* 146, 2147–2159. <https://doi.org/10.1175/MWR-D-17-0320.1>.
- Xu, W.X., Jiang, H.Y., Kang, X.B., 2014. Rainfall asymmetries of tropical cyclones prior to, during, and after making landfall in South China and Southeast United States. *Atmos. Res.* 139, 18–26. <https://doi.org/10.1016/j.atmosres.2013.12.015>.
- Ying, M., Zhang, W., Yu, H., Lu, X.Q., Feng, J.X., Fan, Y.X., et al., 2014. An overview of the China meteorological administration tropical cyclone database. *J. Atmos. Ocean. Technol.* 31 (2), 287–301. <https://doi.org/10.1175/jtech-d-12-00119.1>.
- Yu, Z.F., Yu, H., Gao, S.T., 2010. Terrain impact on the precipitation of landfalling Typhoon Talim. *J. Trop. Meteorol.* 16 (2), 115–124. <https://doi.org/10.3969/j.issn.1006-8775.2010.02.003>.
- Yu, Z.F., Wang, Y.Q., Xu, H.M., 2015. Observed rainfall asymmetry in tropical cyclones making landfall over China. *J. Appl. Meteorol. Climatol.* 54 (1), 117–136. <https://doi.org/10.1175/jamc-d-13-0359.1>.
- Yu, Z.F., Wang, Y.Q., Xu, H.M., Davidson, N., Chen, Y.D., Chen, Y.M., et al., 2017. On the relationship between intensity and rainfall distribution in tropical cyclones making landfall over China. *J. Appl. Meteorol. Climatol.* 56 (10), 2883–2901. <https://doi.org/10.1175/jamc-d-16-0334.1>.
- Zhang, X.B., 2019. Multiscale characteristics of different-source perturbations and their interactions for convection-permitting ensemble forecasting during SCMREX. *Mon. Weather Rev.* 147 (1), 291–310. <https://doi.org/10.1175/mwr-d-18-0218.1>.
- Zhang, J.A., Nolan, D.S., Rogers, R.F., 2019. Effects of parameterized boundary layer structure on Hurricane Rapid intensification in shear. *Mon. Weather Rev.* 147, 853–871. <https://doi.org/10.1175/mwr-d-18-0010.1>.
- Zhang, J.A., Nolan, D.S., Rogers, R.F., Tallapragada, V., 2015. Evaluating the impact of improvements in the boundary layer parameterization on Hurricane intensity and structure forecasts in HWRF. *Mon. Weather Rev.* 143, 3136–3155. <https://doi.org/10.1175/mwr-d-14-00339.1>.
- Zhu, T., Zhang, D.L., 2006. Numerical simulation of Hurricane Bonnie (1998). Part II: sensitivity to varying cloud microphysical processes. *J. Atmos. Sci.* 63 (1), 109–126. <https://doi.org/10.1175/jas3599.1.FO>.
- Zhu, P., Menelau, K., Zhu, Z., 2014. Impact of subgrid-scale vertical turbulent mixing on eyewall asymmetric structures and mesovortices of hurricanes. *Q. J. R. Meteorol. Soc.* 140 (679), 416–438.